

AD-A098 113

HUGHES RESEARCH LABS, MALIBU CA
BASIC PROBLEMS IN INP TECHNOLOGY. (U)

MAR 81 K V VAIDYANATHAN, H L DUNLAP

F/G 20/12

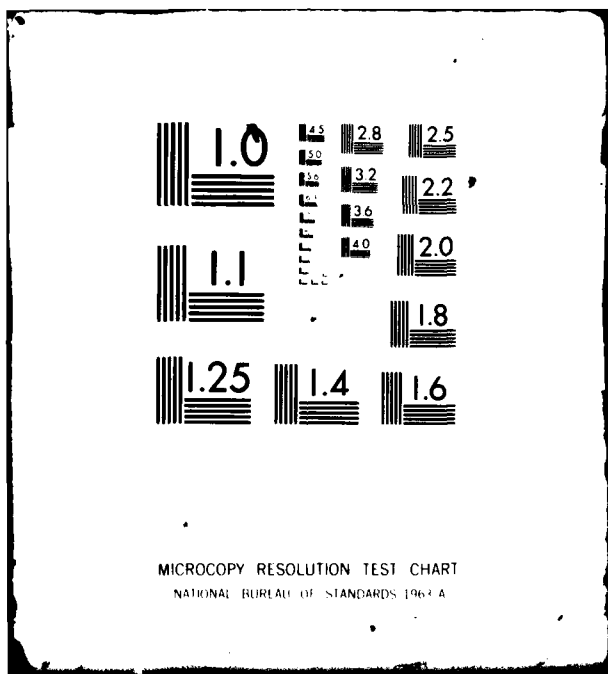
F49620-80-C-0038

NL

UNCLASSIFIED

AFOSR-TR-81-0405

END
DATE
FILED
5-81
DTIC



AD A 098 113

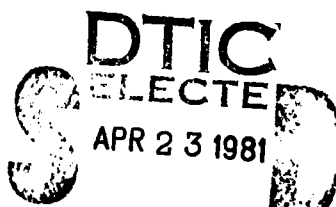
BASIC PROBLEMS IN InP TECHNOLOGY

K.V. Vaidyanathan, H.L. Dunlap, R.A. Jullens, and C.L. Anderson

Hughes Research Laboratories
3011 Malibu Canyon Road
Malibu, CA 90265

March 1981

F49620-80-C-0038
Final Report
For period 16 November 1979 to 15 November 1980



AIR FORCE OFFICE OF SCIENTIFIC RESEARCH
Bolling Air Force Base, D.C. 20332

DTIC FILE NUMBER

81 4 22 035

Approved for public release;
distribution unlimited.

Unclassified

SECURITY CLASSIFICATION OF THIS PAGE (When Data Entered)

1 REPORT DOCUMENTATION PAGE			READ INSTRUCTIONS BEFORE COMPLETING FORM
1. REPORT NUMBER 18 AFOSR/TR-81-0405 ADA098113	2. GOVT ACCESSION NO. 18 AFOSR/TR-81-0405 ADA098113	3. RECIPIENT'S CATALOG NUMBER	
4. TITLE (and Subtitle) 6 Basic Problems in InP Technology.	5. TYPE OF REPORT & PERIOD COVERED 9 Final Report 16 Nov 79-15 Nov 80		
6. AUTHOR(s) 10 K.V. Vaidyanathan H.L. Dunlap R.A. Jullens C.L. Anderson	7. CONTRACT OR GRANT NUMBER(s) 15 F49620-80-C-0038		
8. PERFORMING ORGANIZATION NAME AND ADDRESS Hughes Research Laboratories	9. PROGRAM ELEMENT PROJECT, TASK AREA & WORK UNIT NUMBERS 17 B2 61102 16 2306/B2		
10. CONTROLLING OFFICE NAME AND ADDRESS Air Force Office of Scientific Research Bolling Air Force Base, D.C. 20332	11. REPORT DATE 11 March 81		
12. MONITORING AGENCY NAME & ADDRESS if different from Controlling Office 12 51	13. NUMBER OF PAGES 55		
14. DISTRIBUTION STATEMENT (of this Report) Approved for public release; distribution unlimited.	15. SECURITY CLASS (of this report) Unclassified		
16. DISTRIBUTION STATEMENT (of the abstract entered in Block 19, if different from Report)	17. SECURITY CLASSIFICATION DOWNGRADING SCHEDULE		
18. SUPPLEMENTARY NOTES			
19. KEY WORDS (Continue on reverse side if necessary and identify by block number) InP ion implantation, InP encapsulation, InP liquid phase epitaxy InP ohmic contacts, InP electrical properties, InP photoluminescence			
20. ABSTRACT (Continue on reverse side if necessary and identify by block number) <p>The growth and characterization of high-purity epitaxial InP layers grown by liquid phase epitaxy are described. Silicon and sulfur will be the dominant residual donors in LPE-grown InP. Techniques to reduce the residual donor concentration in the LPE layers are discussed. Chemical polishing and mesa etching of InP and ohmic contact studies to n- and p-type InP are discussed. Preliminary investigations</p>	→ <i>Sh</i>		

Unclassified

SECURITY CLASSIFICATION OF THIS PAGE (When Data Entered)

50,000 W/cm² sq. cm

show that at power densities of 5×10^4 W/cm² permanent laser-induced surface damage occurs in InP. Thus laser-annealed ohmic contacts need to be formed at power densities 5×10^3 W/cm².

Severe surface degradation was observed in SiO₂ encapsulated, ion-implanted InP samples annealed at 700°C. The use of phosphorus-doped glass (PSG) dramatically reduces such surface degradation. The electrical properties of Be and Si-implanted layers are reported as functions of both implantation dose and anneal temperature. Preliminary secondary ion mass spectrometry (SIMS) studies show that at high concentrations dramatic redistribution effects occur in Be-implanted and annealed InP, while no significant diffusion occurs in Si-implanted and annealed InP.

11

Unclassified

SECURITY CLASSIFICATION OF THIS PAGE (When Data Entered)

TABLE OF CONTENTS

SECTION	PAGE
LIST OF ILLUSTRATIONS	5
1 INTRODUCTION AND SUMMARY	7
2 EPITAXIAL GROWTH OF InP	11
3 PROCESS TECHNOLOGY AND OHMIC CONTACT STUDIES	23
4 ION IMPLANTATION STUDIES	31
A. Dielectric Deposition Studies	31
B. Be-Implanted InP	40
C. Si-Implanted InP	45
D. Damage Studies	45
E. Rutherford Backscattering Studies	48
5 SUMMARY	53
REFERENCES	55

1. Color
2. Material
3. Size
4. Orientation
5. Surface
6. Markings
7. Condition
8. Weight
9. Volume
10. Temperature
11. Humidity
12. Pressure
13. Electromagnetic fields
14. Chemical substances
15. Microorganisms
16. UV radiation
17. Gamma radiation
18. Alpha radiation
19. Neutron radiation
20. Proton radiation
21. Neutrino radiation
22. Dark matter
23. Dark energy
24. Dark radiation
25. Dark photons
26. Dark leptons
27. Dark fermions
28. Dark nuclei
29. Dark molecules
30. Dark atoms
31. Dark nuclei
32. Dark molecules
33. Dark atoms
34. Dark nuclei
35. Dark molecules
36. Dark atoms
37. Dark nuclei
38. Dark molecules
39. Dark atoms
40. Dark nuclei
41. Dark molecules
42. Dark atoms
43. Dark nuclei
44. Dark molecules
45. Dark atoms
46. Dark nuclei
47. Dark molecules
48. Dark atoms
49. Dark nuclei
50. Dark molecules
51. Dark atoms
52. Dark nuclei
53. Dark molecules
54. Dark atoms
55. Dark nuclei
56. Dark molecules
57. Dark atoms
58. Dark nuclei
59. Dark molecules
60. Dark atoms
61. Dark nuclei
62. Dark molecules
63. Dark atoms
64. Dark nuclei
65. Dark molecules
66. Dark atoms
67. Dark nuclei
68. Dark molecules
69. Dark atoms
70. Dark nuclei
71. Dark molecules
72. Dark atoms
73. Dark nuclei
74. Dark molecules
75. Dark atoms
76. Dark nuclei
77. Dark molecules
78. Dark atoms
79. Dark nuclei
80. Dark molecules
81. Dark atoms
82. Dark nuclei
83. Dark molecules
84. Dark atoms
85. Dark nuclei
86. Dark molecules
87. Dark atoms
88. Dark nuclei
89. Dark molecules
90. Dark atoms
91. Dark nuclei
92. Dark molecules
93. Dark atoms
94. Dark nuclei
95. Dark molecules
96. Dark atoms
97. Dark nuclei
98. Dark molecules
99. Dark atoms
100. Dark nuclei
101. Dark molecules
102. Dark atoms
103. Dark nuclei
104. Dark molecules
105. Dark atoms
106. Dark nuclei
107. Dark molecules
108. Dark atoms
109. Dark nuclei
110. Dark molecules
111. Dark atoms
112. Dark nuclei
113. Dark molecules
114. Dark atoms
115. Dark nuclei
116. Dark molecules
117. Dark atoms
118. Dark nuclei
119. Dark molecules
120. Dark atoms
121. Dark nuclei
122. Dark molecules
123. Dark atoms
124. Dark nuclei
125. Dark molecules
126. Dark atoms
127. Dark nuclei
128. Dark molecules
129. Dark atoms
130. Dark nuclei
131. Dark molecules
132. Dark atoms
133. Dark nuclei
134. Dark molecules
135. Dark atoms
136. Dark nuclei
137. Dark molecules
138. Dark atoms
139. Dark nuclei
140. Dark molecules
141. Dark atoms
142. Dark nuclei
143. Dark molecules
144. Dark atoms
145. Dark nuclei
146. Dark molecules
147. Dark atoms
148. Dark nuclei
149. Dark molecules
150. Dark atoms
151. Dark nuclei
152. Dark molecules
153. Dark atoms
154. Dark nuclei
155. Dark molecules
156. Dark atoms
157. Dark nuclei
158. Dark molecules
159. Dark atoms
160. Dark nuclei
161. Dark molecules
162. Dark atoms
163. Dark nuclei
164. Dark molecules
165. Dark atoms
166. Dark nuclei
167. Dark molecules
168. Dark atoms
169. Dark nuclei
170. Dark molecules
171. Dark atoms
172. Dark nuclei
173. Dark molecules
174. Dark atoms
175. Dark nuclei
176. Dark molecules
177. Dark atoms
178. Dark nuclei
179. Dark molecules
180. Dark atoms
181. Dark nuclei
182. Dark molecules
183. Dark atoms
184. Dark nuclei
185. Dark molecules
186. Dark atoms
187. Dark nuclei
188. Dark molecules
189. Dark atoms
190. Dark nuclei
191. Dark molecules
192. Dark atoms
193. Dark nuclei
194. Dark molecules
195. Dark atoms
196. Dark nuclei
197. Dark molecules
198. Dark atoms
199. Dark nuclei
200. Dark molecules
201. Dark atoms
202. Dark nuclei
203. Dark molecules
204. Dark atoms
205. Dark nuclei
206. Dark molecules
207. Dark atoms
208. Dark nuclei
209. Dark molecules
210. Dark atoms
211. Dark nuclei
212. Dark molecules
213. Dark atoms
214. Dark nuclei
215. Dark molecules
216. Dark atoms
217. Dark nuclei
218. Dark molecules
219. Dark atoms
220. Dark nuclei
221. Dark molecules
222. Dark atoms
223. Dark nuclei
224. Dark molecules
225. Dark atoms
226. Dark nuclei
227. Dark molecules
228. Dark atoms
229. Dark nuclei
230. Dark molecules
231. Dark atoms
232. Dark nuclei
233. Dark molecules
234. Dark atoms
235. Dark nuclei
236. Dark molecules
237. Dark atoms
238. Dark nuclei
239. Dark molecules
240. Dark atoms
241. Dark nuclei
242. Dark molecules
243. Dark atoms
244. Dark nuclei
245. Dark molecules
246. Dark atoms
247. Dark nuclei
248. Dark molecules
249. Dark atoms
250. Dark nuclei
251. Dark molecules
252. Dark atoms
253. Dark nuclei
254. Dark molecules
255. Dark atoms
256. Dark nuclei
257. Dark molecules
258. Dark atoms
259. Dark nuclei
260. Dark molecules
261. Dark atoms
262. Dark nuclei
263. Dark molecules
264. Dark atoms
265. Dark nuclei
266. Dark molecules
267. Dark atoms
268. Dark nuclei
269. Dark molecules
270. Dark atoms
271. Dark nuclei
272. Dark molecules
273. Dark atoms
274. Dark nuclei
275. Dark molecules
276. Dark atoms
277. Dark nuclei
278. Dark molecules
279. Dark atoms
280. Dark nuclei
281. Dark molecules
282. Dark atoms
283. Dark nuclei
284. Dark molecules
285. Dark atoms
286. Dark nuclei
287. Dark molecules
288. Dark atoms
289. Dark nuclei
290. Dark molecules
291. Dark atoms
292. Dark nuclei
293. Dark molecules
294. Dark atoms
295. Dark nuclei
296. Dark molecules
297. Dark atoms
298. Dark nuclei
299. Dark molecules
300. Dark atoms
301. Dark nuclei
302. Dark molecules
303. Dark atoms
304. Dark nuclei
305. Dark molecules
306. Dark atoms
307. Dark nuclei
308. Dark molecules
309. Dark atoms
310. Dark nuclei
311. Dark molecules
312. Dark atoms
313. Dark nuclei
314. Dark molecules
315. Dark atoms
316. Dark nuclei
317. Dark molecules
318. Dark atoms
319. Dark nuclei
320. Dark molecules
321. Dark atoms
322. Dark nuclei
323. Dark molecules
324. Dark atoms
325. Dark nuclei
326. Dark molecules
327. Dark atoms
328. Dark nuclei
329. Dark molecules
330. Dark atoms
331. Dark nuclei
332. Dark molecules
333. Dark atoms
334. Dark nuclei
335. Dark molecules
336. Dark atoms
337. Dark nuclei
338. Dark molecules
339. Dark atoms
340. Dark nuclei
341. Dark molecules
342. Dark atoms
343. Dark nuclei
344. Dark molecules
345. Dark atoms
346. Dark nuclei
347. Dark molecules
348. Dark atoms
349. Dark nuclei
350. Dark molecules
351. Dark atoms
352. Dark nuclei
353. Dark molecules
354. Dark atoms
355. Dark nuclei
356. Dark molecules
357. Dark atoms
358. Dark nuclei
359. Dark molecules
360. Dark atoms
361. Dark nuclei
362. Dark molecules
363. Dark atoms
364. Dark nuclei
365. Dark molecules
366. Dark atoms
367. Dark nuclei
368. Dark molecules
369. Dark atoms
370. Dark nuclei
371. Dark molecules
372. Dark atoms
373. Dark nuclei
374. Dark molecules
375. Dark atoms
376. Dark nuclei
377. Dark molecules
378. Dark atoms
379. Dark nuclei
380. Dark molecules
381. Dark atoms
382. Dark nuclei
383. Dark molecules
384. Dark atoms
385. Dark nuclei
386. Dark molecules
387. Dark atoms
388. Dark nuclei
389. Dark molecules
390. Dark atoms
391. Dark nuclei
392. Dark molecules
393. Dark atoms
394. Dark nuclei
395. Dark molecules
396. Dark atoms
397. Dark nuclei
398. Dark molecules
399. Dark atoms
400. Dark nuclei
401. Dark molecules
402. Dark atoms
403. Dark nuclei
404. Dark molecules
405. Dark atoms
406. Dark nuclei
407. Dark molecules
408. Dark atoms
409. Dark nuclei
410. Dark molecules
411. Dark atoms
412. Dark nuclei
413. Dark molecules
414. Dark atoms
415. Dark nuclei
416. Dark molecules
417. Dark atoms
418. Dark nuclei
419. Dark molecules
420. Dark atoms
421. Dark nuclei
422. Dark molecules
423. Dark atoms
424. Dark nuclei
425. Dark molecules
426. Dark atoms
427. Dark nuclei
428. Dark molecules
429. Dark atoms
430. Dark nuclei
431. Dark molecules
432. Dark atoms
433. Dark nuclei
434. Dark molecules
435. Dark atoms
436. Dark nuclei
437. Dark molecules
438. Dark atoms
439. Dark nuclei
440. Dark molecules
441. Dark atoms
442. Dark nuclei
443. Dark molecules
444. Dark atoms
445. Dark nuclei
446. <

AIR FORCE OFFICE OF SCIENTIFIC RESEARCH (AFSC)
NOTICE OF TRANSMISSION TO DDC
This technical report has been reviewed and is
approved for public release IAW AFR 190-12 (7b).
Distribution is unlimited.
A. D. BLOSE
Technical Information Officer

LIST OF ILLUSTRATIONS

FIGURE	PAGE
1 LPE growth system	12
2 Epilayer doping concentration versus distance profiles at various points on the wafer shown in the inset	14
3 Graphite slide-bar assembly	15
4 PL spectra of InP	18
5 Depth profile of silicon in InP epitaxial layers obtained by secondary ion mass spectrometry (SIMS) analysis	20
6 Auger electron spectrum obtained from a chemically etched InP sample showing the formation of InO on the surface	25
7 Photomask used to form a mesa to define a transmission line pattern in making contact resistance measurements	26
8 Photomask used to form patterns for evaluating contact resistance of ohmic contacts	27
9 Photomask used to form Schottky barriers to evaluate one doping level of epitaxially grown or ion-implanted layers	28
10 SEM micrograph of InP sample annealed with SiO_2 encapsulant at 700°C for 30 min	33
11 SEM micrograph of InP sample annealed with PSG encapsulant containing 5 at.% P and annealed at 750°C for 30 min	34
12 SEM micrograph of InP sample annealed at 750°C for 30 min with PSG encapsulant (10 at.% P)	35
13 Schematic of the plasma-enhanced deposition system	36
14 RBS spectra of Si_3N_4 films deposited on pyrolytically carbon film	38

FIGURE	PAGE
15 SEM photograph of a sample annealed with Si_3N_4 encapsulant at 700°C for 30 min	39
16 Atomic distribution of ion-implanted Be in InP	41
17 Sheet hole concentration and hole mobility as function of anneal temperature for InP samples implanted with 300 keV Be	42
18 Atomic distribution of ion-implanted Be obtained from unannealed and annealed InP samples showing effects of drastic redistribution	43
19 Sheet electron-concentration as a function of anneal temperature for InP samples implanted with 300 keV silicon to fluences indicated in figure	46
20 Sheet electron concentration as a function of implant fluence for 300 keV Si-implanted InP samples	47
21 Atomic distribution obtained from Si implanted and annealed InP samples	50
22 RBS spectra obtained from InP samples	51
23 Dose versus damage curve for InP implanted with silicon at room temperature	52

SECTION 1

INTRODUCTION AND SUMMARY

Indium Phosphide and related ternary and quaternary compounds exhibit considerably higher steady-state electron velocities at all fields, compared with silicon. This feature, combined with higher electron mobilities achievable in these materials make them attractive for high-speed device applications. The steady-state electron velocity-field characteristics do not take into account any transient effects that can occur in the devices. For example, in short-channel FET devices, the transit time of the carriers between the source and drain regions is short enough (20 to 30 psec) that a steady-state situation may not develop. Instead, a "velocity overshoot" may occur in which the velocity of carriers may significantly exceed the velocity associated with the average electric field between the source and drain. The recent theoretical calculations of Littlejohn et al.¹ indicate that the velocity field characteristics of electrons in InP and InGAs in the presence of velocity overshoot will result in FETs capable of operating at higher frequencies than their GaAs counterparts.

Another major advantage of InP for FET applications is that metal insulator-semiconductor (MIS) structures with low surface-state densities at the semiconductor-insulator interface can be fabricated. Workers at Naval Ocean Systems Center (NOSC) have demonstrated the operation on both enhancement mode and depletion mode InP MISFET devices. Their 4 μm gate enhancement mode devices exhibited 8 dB gain at 1 GHz, while their 1.8 μm depletion mode devices had gains at 16 dB at the same frequency. These preliminary results are extremely encouraging in view of the fact that MESFET devices in InP suffer from the unacceptably low (~ 0.4 eV) Schottky barrier heights attainable on n-type InP. Also, the MISFET devices can typically sustain several volts of forward voltage. This results in considerable relaxation in threshold voltages of individual devices in integrated circuits (ICs) employing these devices. Circuits requiring moderate speeds but very low power, such as Random Access Memories (RAMS) can be easily designed with InP MISFET devices.

InP and InGaAs are promising materials for high speed optoelectronic devices. Lattice-matched InGaAs layers can be grown on InP and have great potential for photodiode applications for 1.0- to 1.6- μ m wavelength range where radiation-resistant optical fibers with very low attenuation and very low dispersion are now available. These fibers will provide the crucial element for long baseline, high speed, secure communication systems. To exploit these potentials, however, semiconductor photo-emitters, photo-detectors, amplifiers, logic circuits, and signal processing devices will be required. High-speed photodetectors of the avalanche or p-i-n type will be one of the critical elements in these systems. Once the MISFET IC technology and the required opto-electronic devices are available, complete integration of the optical system with on-chip signal processing capabilities will be possible. Such systems will be extremely useful for a number of military applications such as the integrated optical spectrum analyzer (IOSA).

To fully exploit the high speed-advantages of InP, it is essential to develop a mature process technology for fabricating devices. All elements of such process technology in InP are in a primitive state. The major areas of investigation, carried out during this one-year program, are listed below and are discussed in subsequent sections.

- In the area of epitaxial growth, we have demonstrated that high-purity, epitaxial layers with device-quality surface morphology can be grown using our infinite solution growth technique. This technique permits us to grow large-area epitaxial layers with reproducible electrical properties and with excellent morphological control. We have also investigated the influence of residual donors in InP such as silicon and sulfur and the control of the concentration of such impurities in the epitaxial layers by the introduction of water vapor in the growth ambient and by prolonged bakeout procedures, respectively.
- We have investigated procedures for encapsulating ion-implanted InP with an appropriate dielectric during the annealing process. These include the evaluation of a plasma-enhanced process for low-temperature deposition of silicon nitride and phosphosilicate glass (PSG) for encapsulation purposes.
- We have studied the electrical activation as well as atomic distribution of silicon (donor) and beryllium (acceptor) implanted layers as a function of anneal parameters in InP. More detailed evaluations of the implanted dopants and defects present in the material will form the focal point for future investigations.

- An area which requires considerable investigation is the formation of ohmic contacts with low contact resistance to lightly doped n- and p-type InP. Most of the common metalizations used for making ohmic contacts to InP (e.g., Au:Ge/Ni to n-InP and Au:Zn to p-InP) require alloying at temperatures in excess of the dissociation point of the material. This presents a severe problem in forming low resistance ohmic contacts. Laser or electron-beam annealing may prove to be the optimum choice for ohmic contact formation in these materials. We have performed some preliminary measurements during this contract period to establish the laser damage threshold in InP. Further experiments on laser-annealed ohmic contacts, including the measurement of specific contact resistance, will be performed.

This report describes the progress in these areas in detail.

SECTION 2

EPITAXIAL GROWTH OF InP

InP, ((In,Ga)As, and (In,Ga)(As,P) layers can be epitaxially grown by a variety of techniques such as liquid-phase epitaxy (LPE),² vapor phase epitaxy (VPE),³ metal organic chemical vapor deposition (MOCVD),⁴ planar reactive deposition (PRD),⁵ and molecular beam epitaxy (MBE).⁶ It appears that LPE offers the best potential for the growth of high-purity InP at this stage.

Two variations of the LPE technique are commonly used: the slide-bar technique using small solutions (the limited melt technique) and the dipping technique using larger solutions (the infinite solution technique). The slide-bar technique has the disadvantage that severe melt depletion effects can occur. Consequently, only a few layers with reproducible properties can be grown from a single melt. This may be a potential problem in the growth of quaternary layers. In contrast, the infinite solution technique, in principle, permits several hundred layers with reproducible properties to be grown from the same melt.

Hughes Research Laboratories (HRL) has developed a unique variation of the infinite solution growth technique. The HRL system illustrated in Figure 1, consists basically of an all-quartz growth tube connected by a high-vacuum valve to a stainless-steel entry chamber. A saturated solution of the appropriate elements serves as the growth matrix. Once a specific solution has been prepared, it is kept in a palladium-purified hydrogen ambient. It can be maintained at or near the growth temperature in a controlled environment for long periods of time. During a long series of runs, all epitaxial growth operations (such as introducing substrates or adding dopants) are performed by passing these materials through an entry chamber, which can be independently evacuated and flushed with hydrogen before opening to the growth tube. It is thus possible to maintain a high-purity solution for a period of months. The growth ambient can also be conveniently changed while keeping all other variables under control. This capability is extremely advantageous in growing high-purity InP layers and is discussed in detail later in this

PRECEDING PAGE BLANK-NOT PLATED

4930 - 7

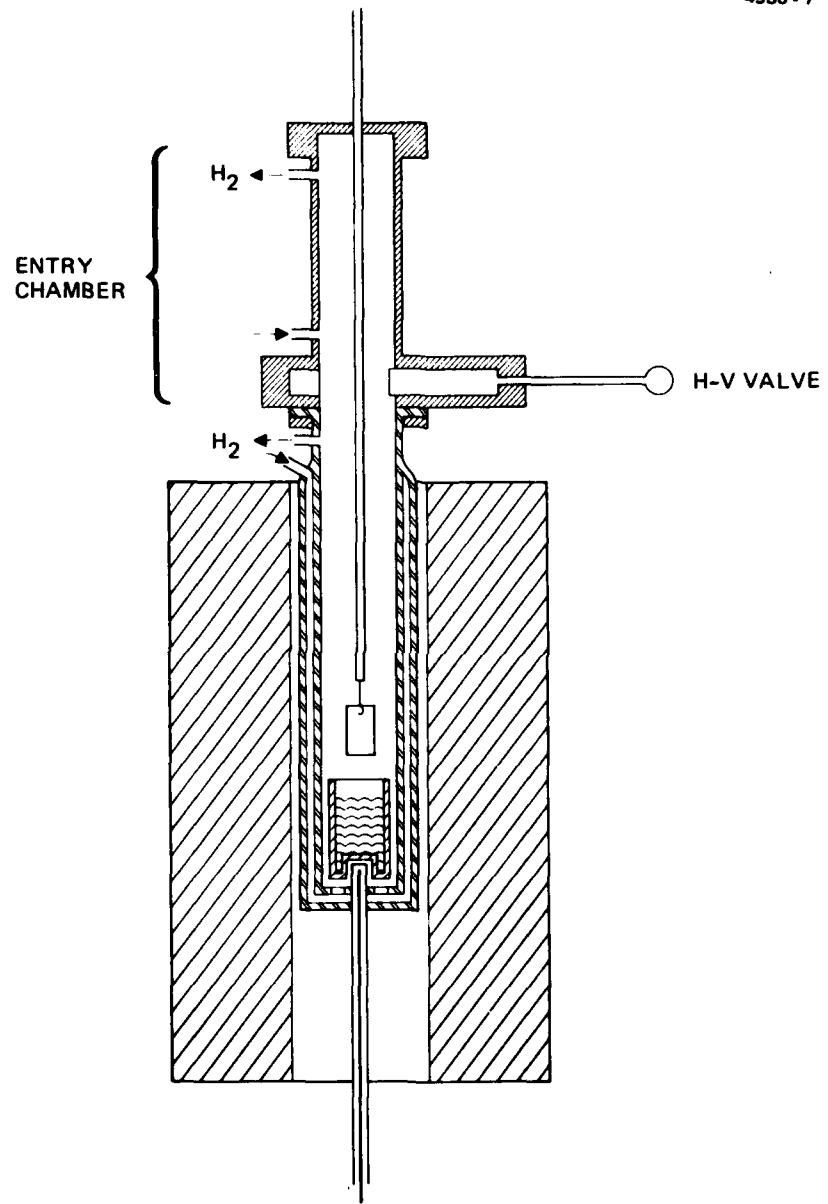


Figure 1. LPE growth system.

section. The InP growth effort was performed under a Hughes internally funded program. Some of the characterization of the epitaxial layers was carried out under this program.

Figure 2 shows the variation in doping concentration as a function of distance into the epitaxial layer grown on a large Sn-doped GaAs wafer (1 x 1-1/4 in., shown in insert) at various points. This represents the doping homogeneity that can be obtained in layers grown by the infinite solution system.

The performance of opto-electronic devices depends critically on the ability to grow uniform, thin, homogeneous and dislocation-free epitaxial layers. Also, in devices involving heterojunctions, it is necessary to reduce defects at the interface. To satisfy all these requirements, the surfaces must see a uniform growth ambient (a chemically homogeneous growth matrix and uniform temperature over the growth surface), and the layers must be grown slowly enough to permit near-equilibrium conditions to be established at the growth interface.

We have developed a graphite sample holder assembly to house the substrate (Figure 3). This permits us to grow the layers under such conditions. The sample holder is introduced into the melt with the substrate inside it, and the whole assembly is rotated in the melt. This permits temperature equilibrium to be fully established. The rotation further helps to ensure good mixing and maintain homogeneity in the melt. The graphite cover was then raised, exposing the sample to the melt. Growth is stopped by (1) closing the cover; (2) raising the sample holder out of the solution; and (3) reopening the cover, at which point the solution trapped in the sample holder falls out. Note that at no time in the growth procedure does the surface of the sample pass through the meniscus of the solution. Furthermore, the cover of the sample holder does not wipe the melt from the sample. Using this technique, we have grown thin epitaxial layers with excellent surface morphology and reproducible electrical properties.

The infinite solution technique has been successfully used to grow high-purity InP layers with carrier concentrations of $\sim 3 \times 10^{15} \text{ cm}^{-3}$ and mobilities of $4,500 \text{ cm}^2 \text{ V}^{-1} \text{ s}^{-1}$ (77°K mobility of $41,000 \text{ cm}^2 \text{ V}^{-1} \text{ s}^{-1}$) reproducibly. We

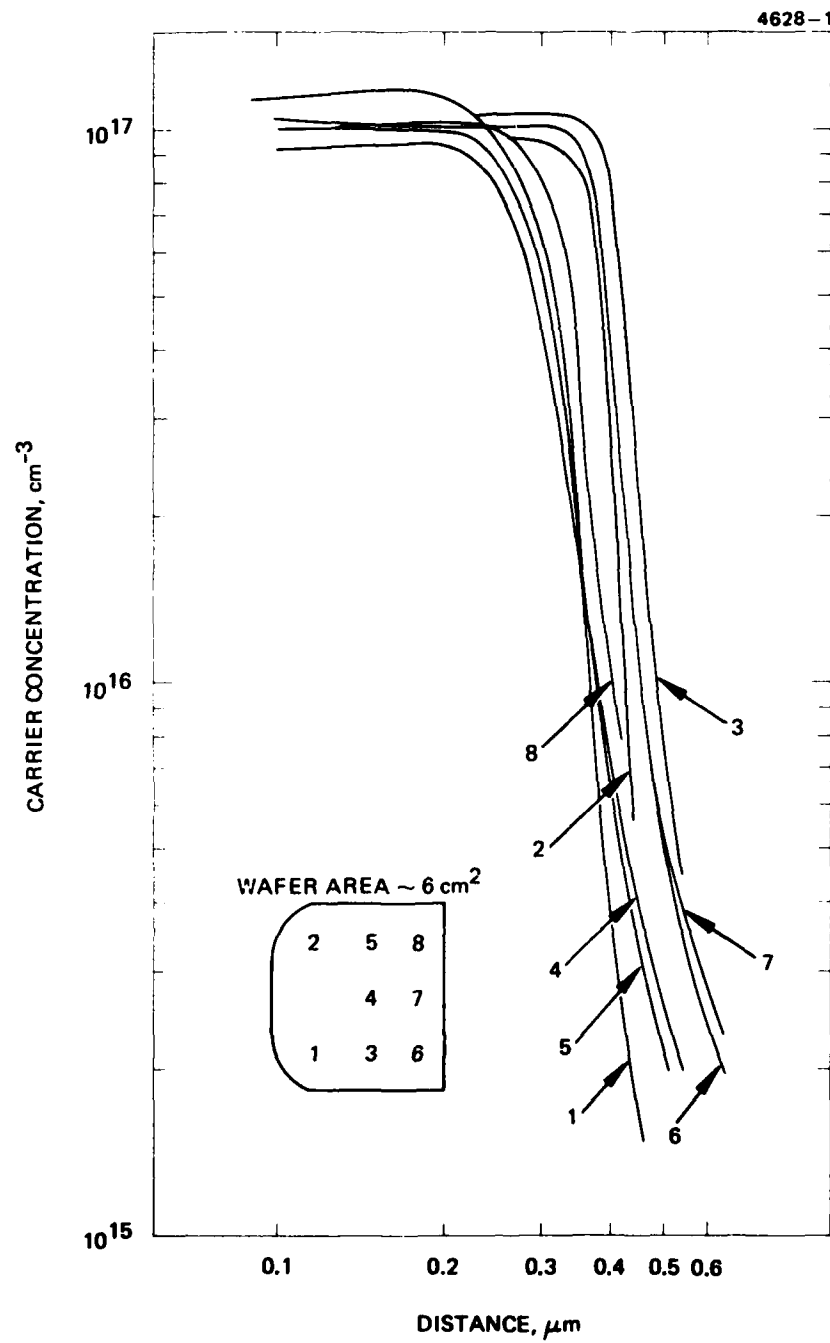


Figure 2. Epilayer doping concentration versus distance profiles at various points on the wafer shown in the inset.

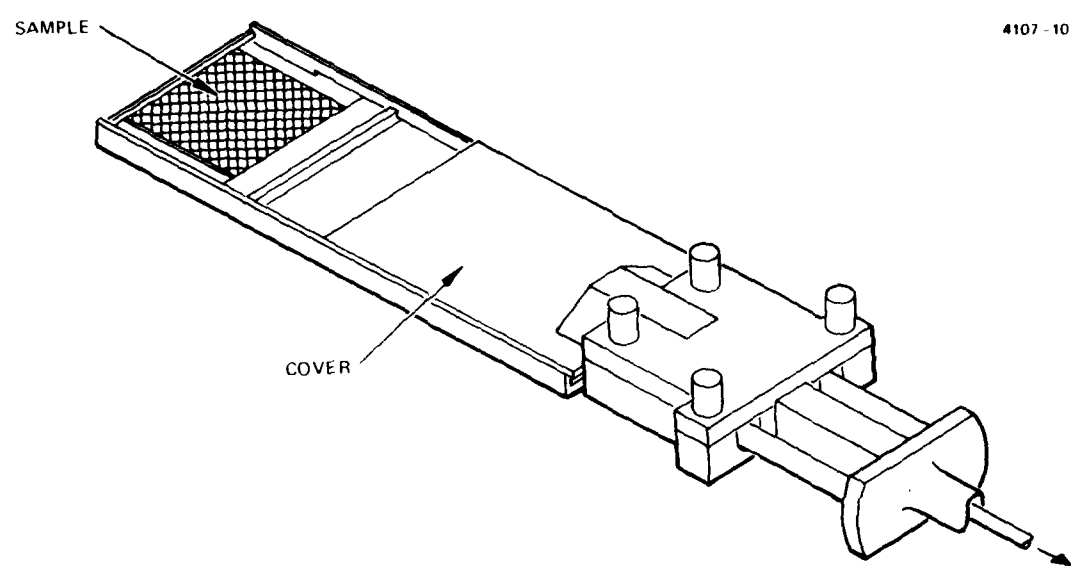


Figure 3. Graphite slide-bar assembly.

have also conducted extensive studies, using internal funds, to study the influence of ~0.1 to 10 ppm of water vapor in the growth ambient. The results of this study are summarized in Table 1. These results can be explained as follows. Silicon is believed to be the dominant residual donor in InP. The quartz in the growth system reacts with H_2 , which reduces it to SiO vapor. The SiO vapor is then reduced by In in solution, which results in Si doping of the solution. Consequently, in the presence of pure H_2 , the Si level in solution reaches an equilibrium level. However, when a small quantity of water vapor is added to the growth ambient, the reduction of quartz by H_2 is suppressed; also, the Si in solution reacts with water vapor, forming SiO vapors. Consequently, the Si level in solution is reduced considerably. This model has been verified by experiments in which layers were grown by turning the water vapor on and off. Under those conditions, net donor concentration cycles: it is high when water vapor is absent and low when it is present.

Extensive Hall-effect measurements have been performed as a function of temperature on the epitaxial layers. Analysis of the data yields the donor (N_D) and acceptor (N_A) concentrations and the degree of compensation. The data clearly show that both N_D and N_A decrease when even small quantities of water vapor are present in the growth ambient. Since Si is the dominant residual impurity, we believe, this evidence indicates the amphoteric nature of Si in InP. This is the first time that the acceptor behavior of Si in InP has been observed. In contrast to the situation with GaAs, this effect is observable in InP only at very low Si concentrations. This, we believe, is a good indication of the purity of our epitaxial layers.

The results of a low-temperature photoluminescence (PL) evaluation of InP epitaxial layers grown in the absence and presence of water vapor in the growth ambient are shown in Figure 4. The sample grown in pure H_2 had a total carrier concentration of $8.5 \times 10^{16} \text{ cm}^{-3}$. The PL spectrum obtained from this sample is dominated by broad emission bands centered at 1.419 and 1.385 eV. The 1.419 eV band is related to band-edge emission and is relatively broad in this sample. The emission at 1.385 eV appears to involve donors and acceptors. In contrast, the spectrum from a sample grown in the presence of

Table 1. Electrical Properties of InP Epitaxial Layers Illustrating the Influence of Water Vapor in the Gas Stream

Sample Number	Ambient	n, cm^{-3} (300°K)	$\mu, \text{cm}^2 \text{V}^{-1}$ sec^{-1} (300°K)
1	Pure hydrogen	1.4×10^{17}	2600
2	Pure hydrogen	2.6×10^{17}	2600
3	Hydrogen + H_2O	2.1×10^{15}	3500
4	Hydrogen + H_2O	2.3×10^{15}	4500
5	Hydrogen + H_2O	4.2×10^{15}	4200
6	Hydrogen + H_2O	2.3×10^{15}	3800
7	Hydrogen + H_2O	2.5×10^{15}	4100
8	Hydrogen + H_2O	2.9×10^{15}	4100
9	Pure hydrogen	1.1×10^{16}	3700
10	Pure hydrogen	6.1×10^{16}	3100
11	Pure hydrogen	1.1×10^{17}	3200
12	Hydrogen + H_2O	2.3×10^{15}	4200

T7440

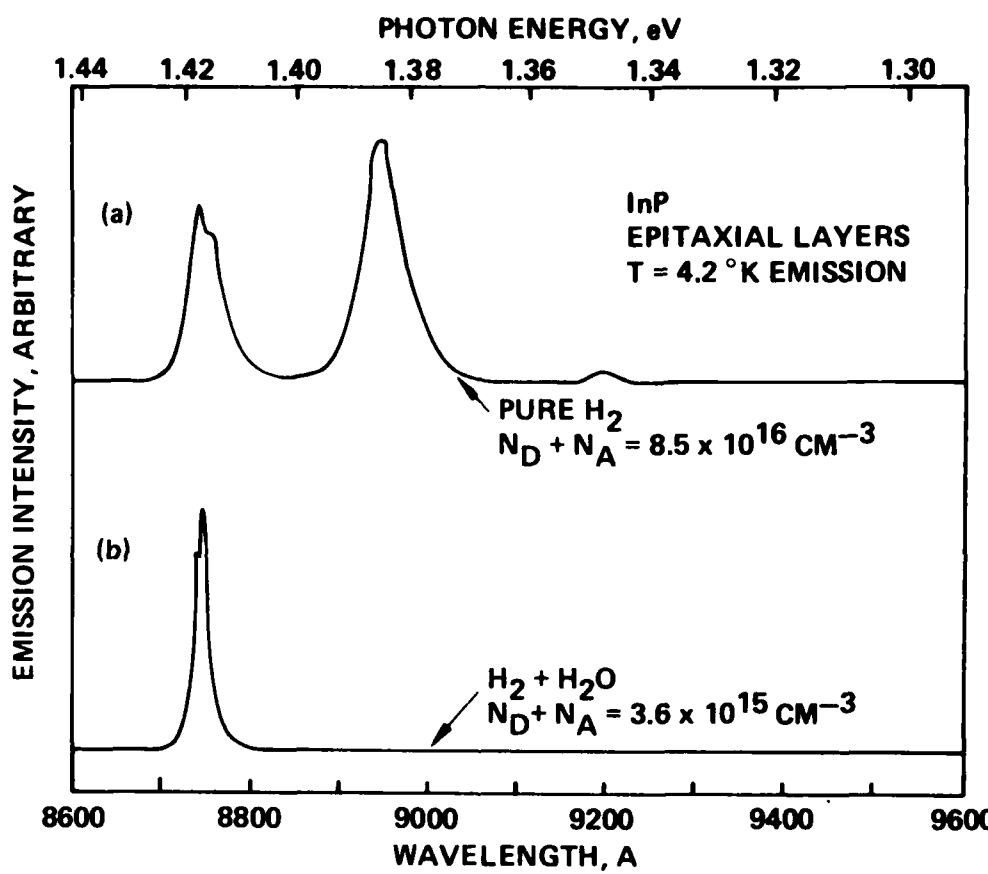


Figure 4. PL spectra of InP.

water vapor exhibits a narrower edge emission (1.419 eV) and an absence of the donor-acceptor emission. The electrical and optical evaluations discussed above show that the samples grown in the presence of water vapor are indeed of higher purity than the ones grown in a H_2 ambient (with no water vapor present).

We have also performed secondary ion mass spectrometry (SIMS) studies on InP liquid epilayers grown in H_2 ambient as well as in samples grown in the presence of water vapor. By using Cs ions as the primary bombarding species, it has been demonstrated that the detection sensitivity for Si and other group IV elements can be improved. As seen from the data in Figure 5, it is clear that layers grown in the presence of water vapor contain smaller quantities of Si as an impurity. Similar results were also obtained from Auger electron spectroscopy (AES) studies. The chemical studies mentioned above, in conjunction with the electrical data presented earlier, clearly demonstrate that the incorporation of Si resulting from the reduction of quartz is indeed an important source of donors in LPE-grown InP.

During these investigations, we observed that not all solutions responded in the same fashion (quantitatively) to the addition of water vapor. Carrier concentrations 2 to $3 \times 10^{16} \text{ cm}^{-3}$ were measured when layers were grown from some solutions in the presence of water vapor in the growth ambient. These results led us to believe that an additional donor may be present in the starting solution and consequently in the grown layers. Detailed mass spectrometry analysis of such layers reveal the presence of considerable quantities of S. The S contamination may either come from the starting polycrystalline material or from some other source of contamination, such as the graphite sample holder. We are presently investigating the source of the S contamination.

Since the vapor pressure of S is quite high, the S contamination can be reduced by baking the growth solution at elevated temperatures. Such a bakeout followed by growth in the presence of water vapor at a temperature lower than the bakeout temperature can be used to grow high purity InP layers even from an originally contaminated solution.

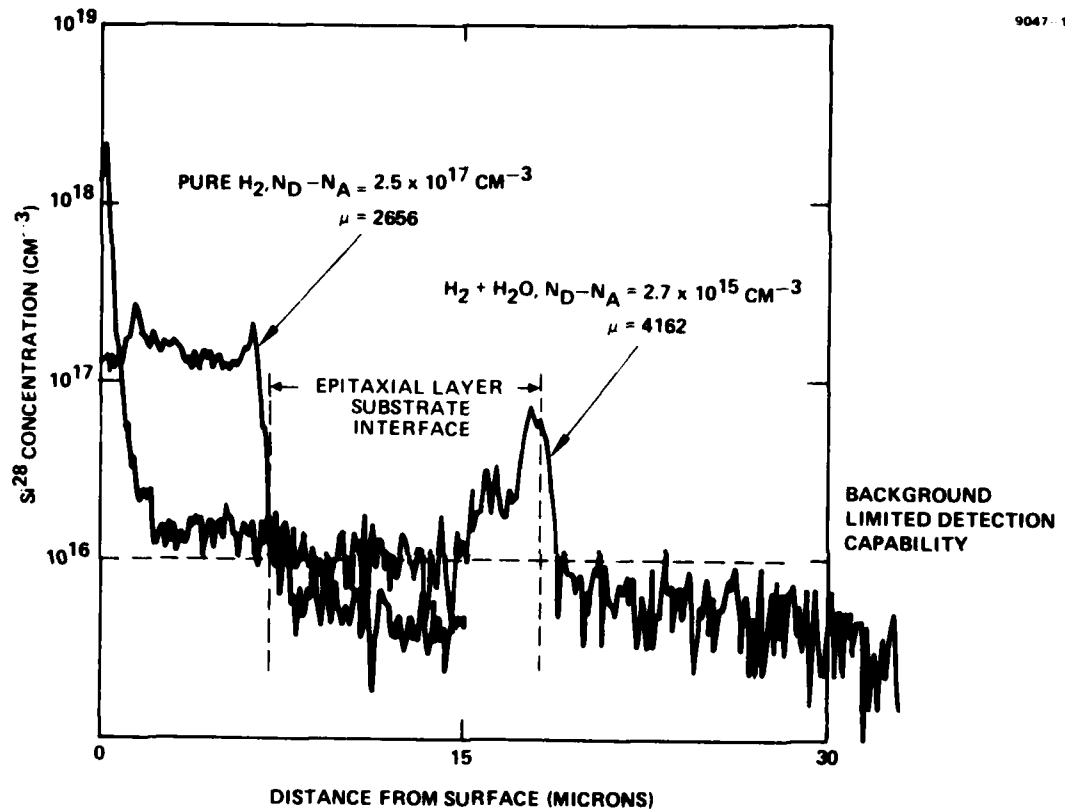


Figure 5. Depth profile of silicon in InP epitaxial layers obtained by secondary ion mass spectrometry (SIMS) analysis.

After establishing the criteria for high-purity growth, we will counter-dope the solution with controlled quantities of acceptors to result in the growth of highly doped p-type layers with hole mobilities in excess of $200 \text{ cm}^2 \text{ V}^{-1} \text{ sec}^{-1}$. To grow several layers with reproducible properties, it will be necessary to choose an acceptor exhibiting low vapor pressure. We have successfully demonstrated the p-type GaAs and (Al, Ga)As layers can be grown using either Be or Ge as an acceptor dopant. We will use either one of them as a dopant of choice for the growth of p-type InP.

SECTION 3

PROCESS TECHNOLOGY AND OHMIC CONTACT STUDIES

In the area of discrete device processing, it is necessary to develop processes for etching mesas during the fabrication of mesa-type FETs and Gunn devices. Mesa-type FETs require mesas with tapered edges to permit their gate lines to cross from the active area to the semi-insulating substrate without breaking. In this application, no metal is present on the device surface at the time of etching. Thus, there is wide latitude in the etchants that may be used.

To perform the mesa etching for FET devices, we have investigated the use of 5% bromine methanol and of a mixture of 1:1:6:1 of HAC:HC1O₃:HNO₃:HC1. The latter etch results in a relatively smooth surface, and consequently the mesa is not rough-sided. We have also developed a technique for jet etching and thinning InP samples by using a 2% solution of bromine in methanol.

In defining mesas for Gunn-effect devices, however, the ohmic contact metal is commonly used as an etch mask. Ideally, the ohmic contact material is plated to a thickness of several micrometers after alloying to form an integral heat sink before mesa definition. The wafer is then processed into discrete devices by etching rather than scribing and breaking. This reduces mechanical stress on the devices and permits the use of plated rather than ultrasonically bonded contacts to the alloyed metal. This approach leads to minimum thermal resistance and increased device reliability.

The primary difficulty with this process is that the Au:Ge or Au:In:Ge alloys most commonly used for contacting the InP material are attacked by hydrobromic acid, which generally is used for mesa definition. We will investigate various combinations of ohmic contact materials and etchants to find an optimum combination for InP device work. Because Au:In:Ge is a very good ohmic contact material for InP, we will search first for better etchants. Aqueous iron chloride solutions are compatible with Au:In:Ge but produce rough-sided mesas. Both HBr-based and FeCl₃ etches are an isotropic and therefore do not produce circular mesas.

~~PRECEDING PAGE BLANK-NOT PAP~~

We have developed a masking technique for etching InP with hydrobromic acid in the presence of Au:Ge ohmic contacts. After defining the ohmic contact and alloying it at 400°C, a layer of silicon oxynitride is deposited over the sample by the plasma-enhanced deposition (PED) process. A thin Pt layer is deposited on top of the silicon oxynitride. Using standard photolithography and lift-off techniques, the $\text{SiO}_{x,y}\text{N}_y$ and Pt layers are left only on top of the ohmic contacts. The mesa etching is then performed using Pt as a mask. Finally, the Pt and $\text{SiO}_{x,y}\text{N}_y$ are removed by dissolving in dilute HF, thus completing the processing step. The preliminary results are promising.

During etching of the deep mesa (>20 μm) required for Gunn devices, the etch rate (regardless of the etchant used) almost always drops considerably after the first few minutes. Auger electron spectroscopy (AES) analysis of the etched surface reveals that a film of stable indium oxide is formed, which retards further chemical reaction. A typical AES spectrum is shown in Figure 6. A combination of dry chemical etching (such as plasma etching) in combination with the conventional wet chemical processes may well solve the problem.

As discussed above, the major problem with mesa etching for Gunn diodes arises from the incompatibility between the metalization and the wet chemical etches commonly used. To solve this problem, we propose to investigate a variety of metalizations involving novel approaches, dry chemical processes such as plasma etching, and various wet chemical etches.

Little information exists as to ways of making low-resistance ohmic contacts to lightly doped n- and p-type InP. The ability to form such contacts will be invaluable in fabricating small-geometry FET devices. During the past few months, we have evaluated the applicability of two metalization schemes: one for n-type InP and the other for lightly doped p-type InP. We have also designed a set of masks that will permit us to photolithographically define metalization patterns. Using these patterns, we can evaluate the contact resistance to ion-implanted layers, epitaxial layers, and to bulk n- and p-type InP. The masks used shown in Figures 7 through 9, are discussed below.

Figure 7 shows the pattern of the first level of the mask set used in evaluating the contact resistance. This mask will be used to etch an alignment mark on the wafer and also to etch a moat around a mesa. The moat

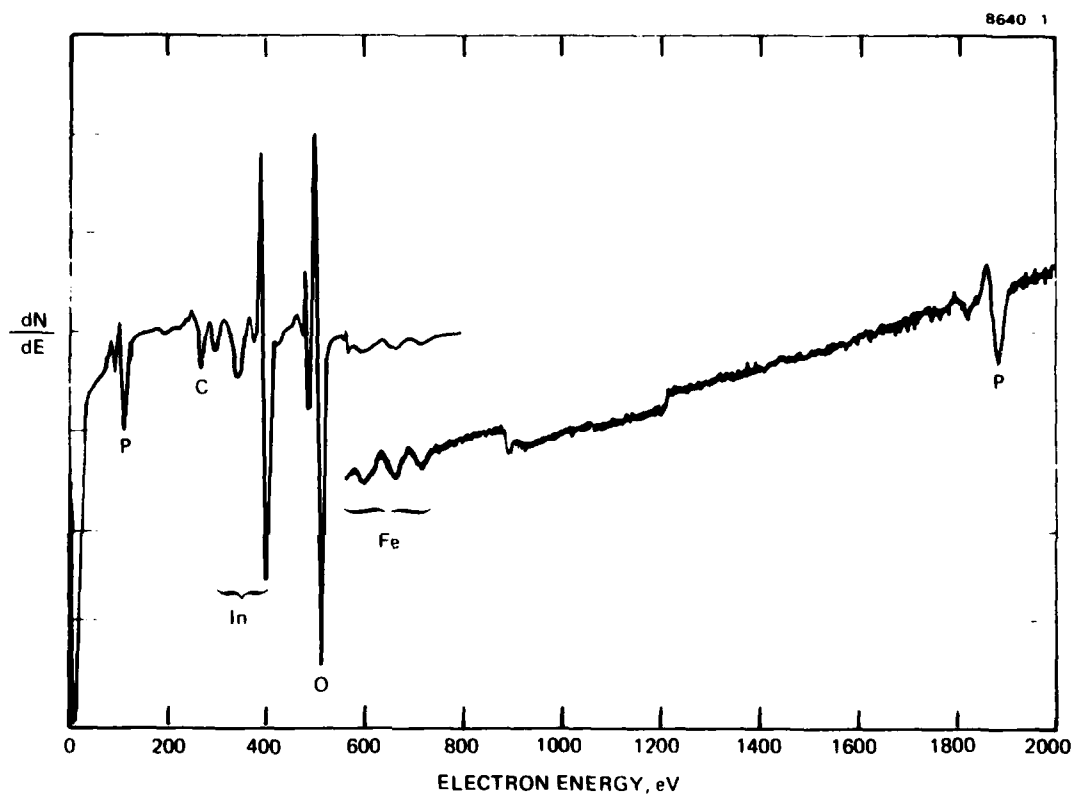


Figure 6. Auger electron spectrum obtained from a chemically etched InP sample showing the formation of In₂O on the surface.

10696-5

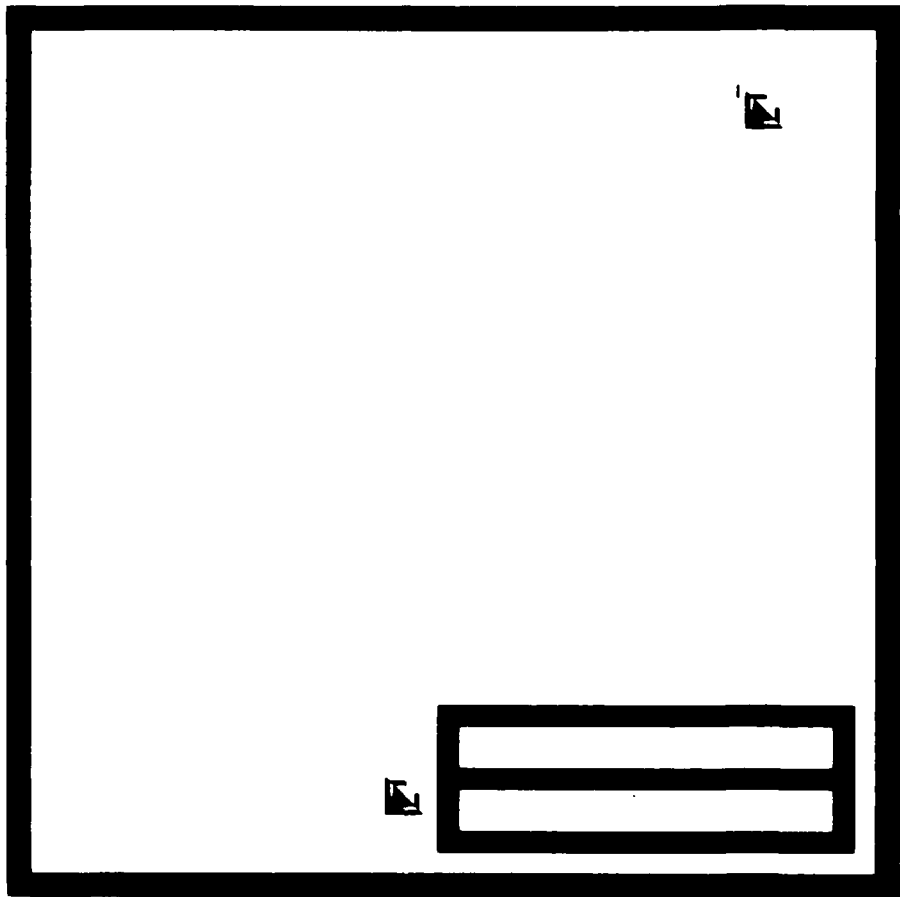


Figure 7. Photomask used to form a mesa to define a transmission line pattern in making contact resistance measurements.

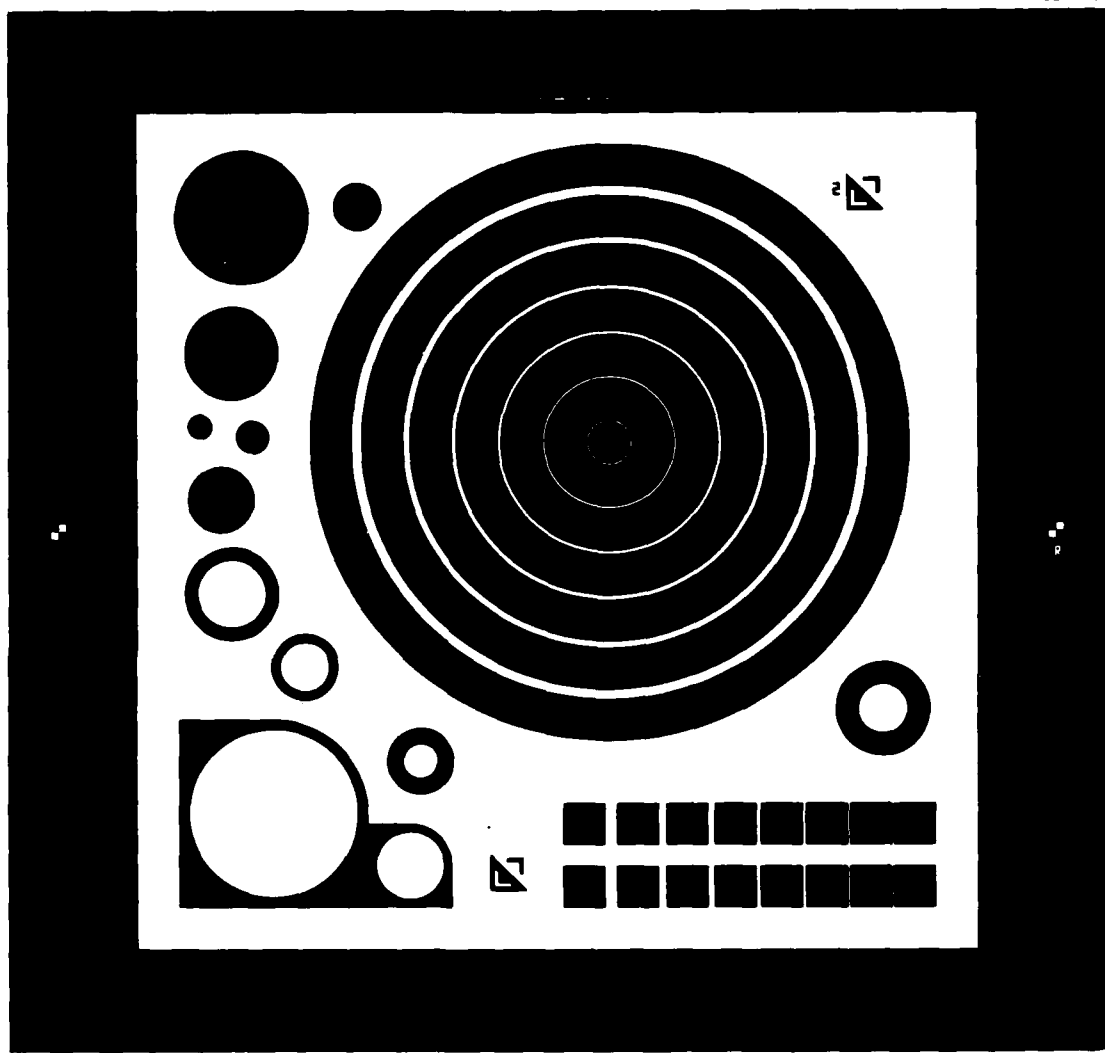


Figure 8. Photomask used to form patterns for evaluating contact resistance of ohmic contacts.

10695-3

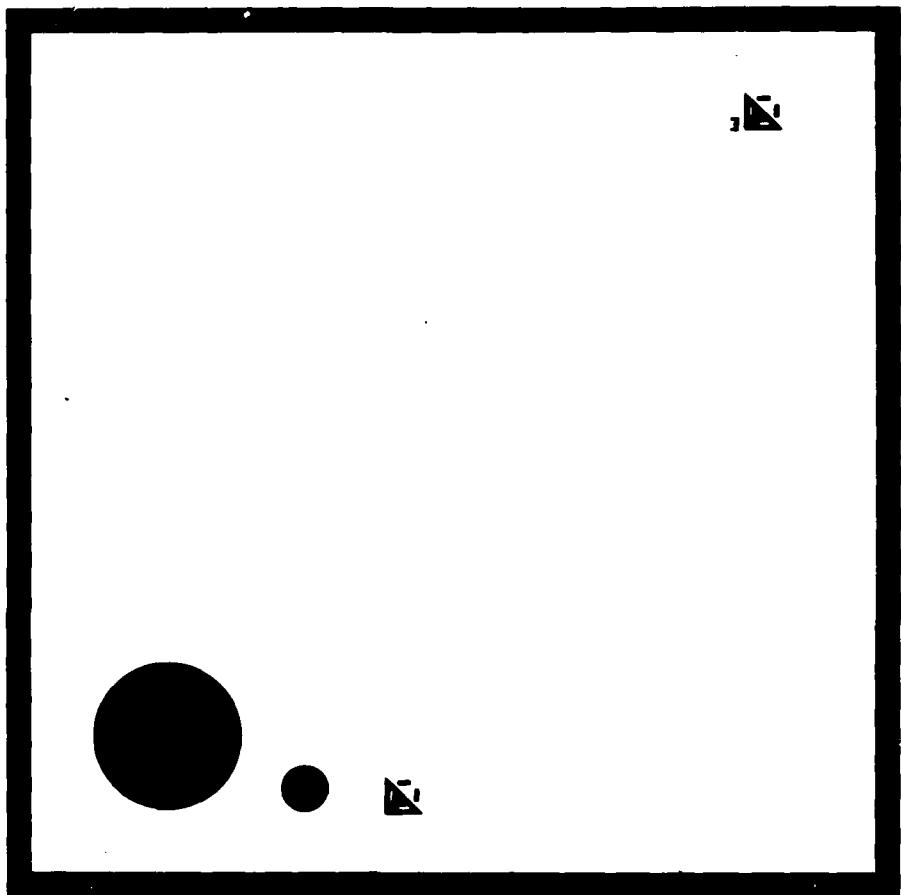


Figure 9. Photomask used to form Schottky barriers to evaluate one doping level of epitaxially grown or ion-implanted layers.

will isolate the mesa (in evaluating the contact resistance to epi- or ion-implanted layers) from the rest of the wafer. The mask shown in Figure 8 will be used to form the metalization pattern defined by the lift-off process. As seen from the figure, a series of metalized regions separated by varying distances will be formed over the mesa. This pattern results in the so-called transmission line method of evaluating the contact resistance. The spacings used in this mask set are 2.5, 5, 7.5, 10, 15, 20, and 30 μm . To estimate the contact resistance, a set of current-voltage (I-V) measurements are made as a function of the spacing between the fingers. A linear least-squares fit is then performed to obtain the intercept on the Y axis and the slope. The contact resistance can then be evaluated.

The evaluation pattern also allows us to fabricate a series of metal dots with different diameters and a series of concentric circles. The concentric-circle pattern is a variation of the transmission-line pattern discussed above but has the added advantage of having a closed geometry, thus alleviating some of the problems associated with fringing of electric fields near the periphery of the pattern. Figure 9 shows the mask which forms a Schottky barrier. This Schottky device will permit us to perform capacitance-voltage (C-V) measurements to evaluate the doping level in the test wafer.

Ohmic contacts to lightly doped p-type InP were formed by sputtering a layer of Au-Zn alloy. Low-resistance ohmic contacts were formed by alloying this metalization in a forming gas atmosphere. To ensure that no surface degradation took place during the sintering process, the samples were coated with a layer of silicon dioxide. The contact resistance of this alloy is presently being measured. On alloying at 350°C, the contacts became ohmic but with extremely high contact resistance. On alloying at 450°C for 5 min., the contact resistance improved. We estimate the contact resistance to be $0.3 \text{ }\mu\text{-cm}^2$

The uncertainty in the absolute value of the contact resistance is fairly high. In arriving at the equations to evaluate the contact resistance, several assumptions have been made. A major assumption is that the conducting layer to which contacts are made is very thin when compared with the dimensions of the contact metalization. This assumption is quite acceptable when dealing

with thin epitaxial or ion-implanted layers. However, when dealing with bulk samples, this assumption is not valid. In such cases, the correction factor involved can be quite large. Our future investigations on ohmic contacts will be performed on epitaxial or ion-implanted layers on semi-insulating InP substrates.

During this reporting period, we have performed some preliminary experiments on laser annealing of InP. We propose to use this technique for ohmic contact formation in this material. From the extensive experience gained from our work on laser-annealed ohmic contacts to GaAs, it is clear that there is a very narrow range of power density over which efficient annealing occurs. This useful range is always slightly lower than the laser damage threshold. At power densities above the damage threshold, severe surface damage (including erosion of the sample) occurs. It is thus essential to experimentally determine the damage threshold for a given semiconductor before any extensive annealing studies can be initiated. From the preliminary studies, we estimate the damage threshold in InP to be $\sim 5.8 \times 10^4$ W/cm² for a scanned CW Ar ion laser. At higher power densities, severe surface damage, including loss of phosphorus, occurs. Having established the damage threshold, we will investigate contact resistance of laser-annealed ohmic contacts on ion-implanted InP layers.

SECTION 4

ION IMPLANTATION STUDIES

To anneal radiation damage and electrically activate the ion-implanted dopants, it is essential to subject the samples to prolonged heat treatment at elevated temperatures. For example, anneal temperatures in excess of 800°C are required to activate most dopants in ion-implanted GaAs. This anneal temperature is above the dissociation temperature of GaAs. In the case of InP, the problem is even more severe because of its much lower dissociation temperature. It is thus essential to develop an appropriate encapsulant capable of preventing surface dissociation or to perform the anneals in a carefully controlled ambient. Our progress in the development of the annealing encapsulant, the electrical properties of the annealed layers, and the atomic distributions in the ion-implanted and annealed layers are discussed in subsequent sections.

A. DIELECTRIC DEPOSITION STUDIES

Hughes Research Laboratories has developed several systems capable of depositing a variety of dielectrics for application to compound semiconductors. The development of these systems and the characterization of the deposited layers have been performed using Hughes internal funds.

Hughes has developed a system capable of depositing dielectric films by a pyrolytic process. The system operates at atmospheric pressure. It consists of a cold-wall reactor into which the reactant gases are metered. The samples are placed on a graphite susceptor, which can be heated inductively by an rf coil surrounding the reactor. This approach has the advantage that the samples can be loaded cold and maintained at temperatures much lower than the dissociation temperature of the sample prior to deposition. The sample temperature can be controlled between 280 to 750°C and the desired sample temperature can be reached within a few seconds. SiO_2 layers were deposited at substrate temperature of 330°C with the following gas flow parameters:

Nitrogen	42 l/min
SiH_4	$11 \text{ cm}^3/\text{min}$
Oxygen	$210 \text{ cm}^3/\text{min}$

The nitrogen provides the necessary flow to keep the reactor flushed and does not participate in the reation. PSG layers were formed by preforming the depositions under the same flow conditions with the addition of $1.9 \text{ cm}^3/\text{min}$ of PH_3 . Typical deposition rates of 70 \AA/min were obtained for PSG layers, and the films exhibited typical index of refraction of 1.45. Energy dispersive x-ray analysis (EDAX) and Auger electron spectroscopy (AES) measurements were performed on the layers deposited with the above flow rates. We estimate the phosphorus content in the films deposited under the above flow conditions to be ~ 5 at %. Increasing the PH_3 flow increases the phosphorus content in the film. We have successfully deposited PSG films containing as high as ~ 8 at % phosphorus.

The surface morphology of InP samples annealed with different encapsulants were examined by a Cambridge 150 Steroscan Scanning Electron Microscope. A sample annealed with SiO_2 encapsulant at 700°C for 30 min exhibited a severe surface degradation as shown in Figure 10. Examination of the sample with the oxide in place revealed cracks in the encapsulant. On removing the oxide, shiny tracks on the surface of the sample were observable. The damaged region on the sample was much wider than the cracks in the oxide. X-ray analysis of the damaged regions reveal considerable loss of phosphorus in these regions. This data indicates that the shiny tracks may be formed by molten and resolidified In.

Figure 11 illustrates the surface morphology observed on a sample annealed with PSG encapsulant (5 at .% P) at 700°C for 30 min. Some rupturing of the encapsulant with the resultant loss of phosphorus was observed. The extent of the damage, however, was much less severe. When the phosphorus content in the PSG layers was increased from 5 to 8%, no noticeable degradation occurred. The surface morphology of this sample is shown in Figure 12. These preliminary studies clearly indicate that the phosphorus content in the PSG layers is critical in the performance of the encapsulant.

Hughes Research Laboratories has also designed and constructed an plasma-enhanced deposition system capable of depositing oxygen-free silicon-nitride layers at temperatures as low as 200°C . A schematic of the system is shown in Figure 13. It consists of a pyrex chamber (9 in. in diameter) evacuated by a diffusion pump and backed by a rotary mechanical pump. The chamber has

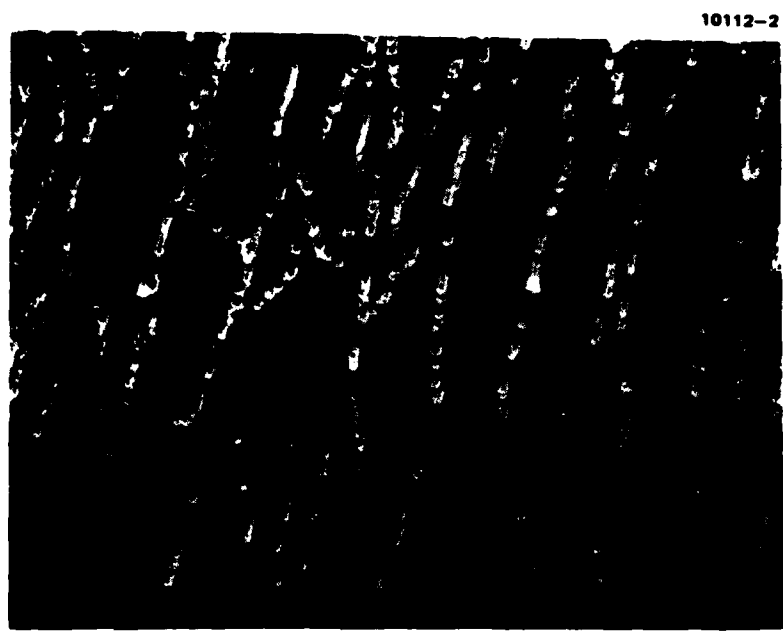


Figure 10. SEM micrograph of InP sample annealed with SiO_2 encapsulant at 700°C for 30 min.

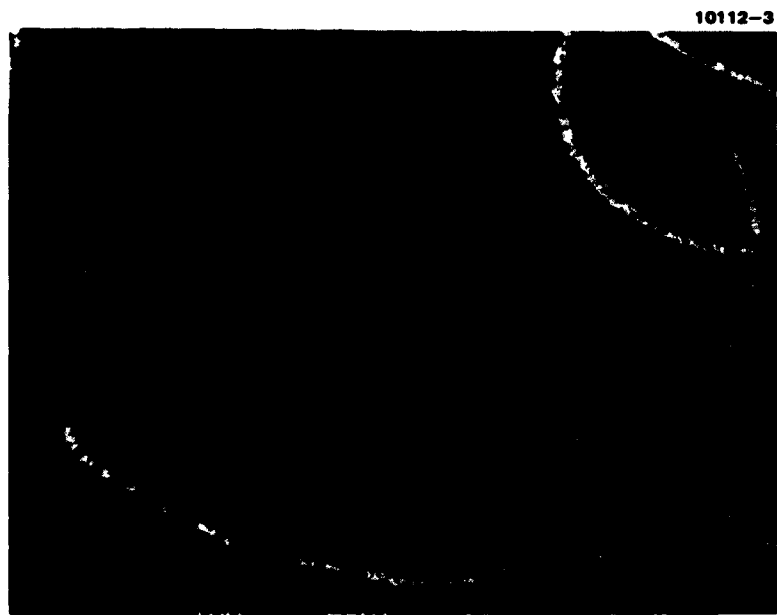


Figure 11. SEM micrograph of InP sample annealed with PSC encapsulant containing 5 at.% P and annealed at 750°C for 30 min.

10112-4

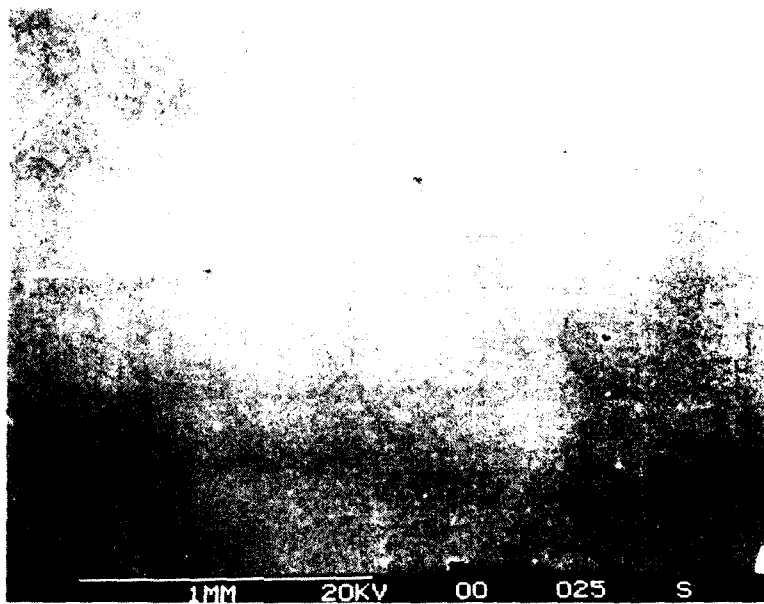


Figure 12. SEM micrograph of InP sample annealed at 750°C for 30 min with PSG encapsulant (10 at. % P). The surface of the implanted and annealed region is of comparable quality to that of an unprocessed wafer.

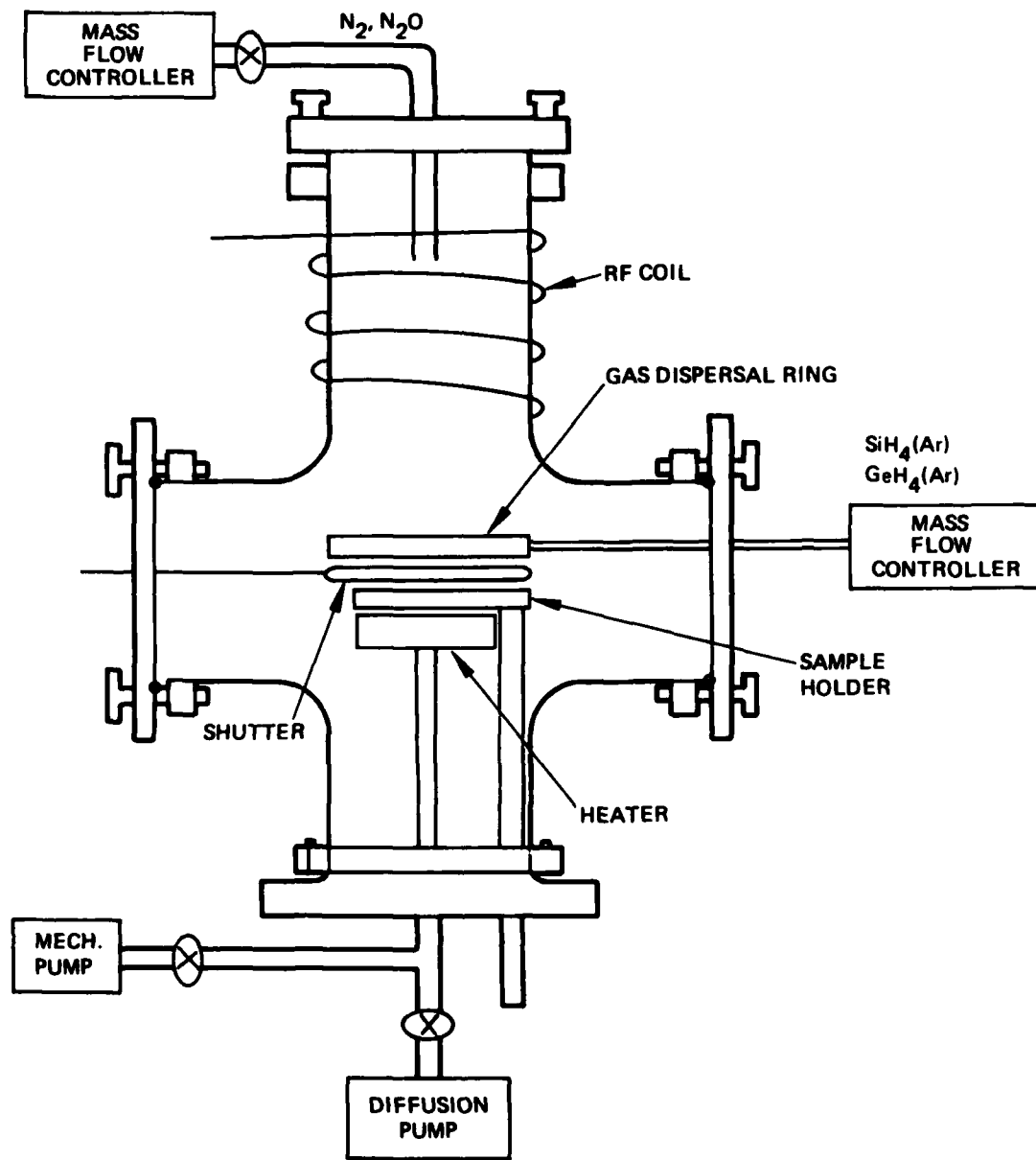


Figure 13. Schematic of the plasma-enhanced deposition system.

three arms, each approximately 9 in. long. The sample holder assembly is physically separate from a heater assembly. The two can be brought into close contact or separated while the system is under vacuum. This feature permits us to load the samples on a cold sample holder and heat them in vacuum in the deposition chamber. The heater assembly is capable of rotating around its axis. The reactant gases are introduced into the system either through the top or from the side of the chamber as shown in Figure 13. The gases introduced from the side flow through a gas dispersal ring which can oscillate across the sample holder in a horizontal plane. The rotational as well as the oscillatory motions homogenize the gas flow in the system, resulting in the deposition of uniformly thick layers across the wafer. The system can be cleaned reactively. There is a shutter which shields the surface of the samples from the plasma during the reactive cleaning process. This system has been used to deposit silicon-nitride layers.

The gas flow and discharge characteristics of the system and their influence on the nature of the deposited layers have been studied in detail. The silicon nitride films exhibit a typical refractive index of ~1.92. Rutherford backscattering studies indicate that there is very little oxygen contamination of these films. A typical backscattered spectrum of a film deposited on a carbon layer on a silicon substrate is shown in Figure 14. The position of the relative edges of the constituents is shown in this figure. The oxygen level in this film is quite low. Most of the oxygen in the film is probably caused by absorbed oxygen on the surface of the nitride layer.

Ion-implanted InP samples encapsulated with Si_3N_4 layers were annealed at 700°C for 30 min. Besides the type of degradation resulting from loss of phosphorus, cracks were observed on the surface of the wafer. These cracks were essentially parallel to each other (Figure 15) and were along the cleavage planes of the wafer. This suggests that the defects are crystallographic. Similar defects were observed in GaAs samples annealed with dense pyrolytic Si_3N_4 layers. These defects arise because of the tensile stresses present in the dielectric encapsulant film. We will compare in detail electrical properties of layers annealed with different encapsulants.

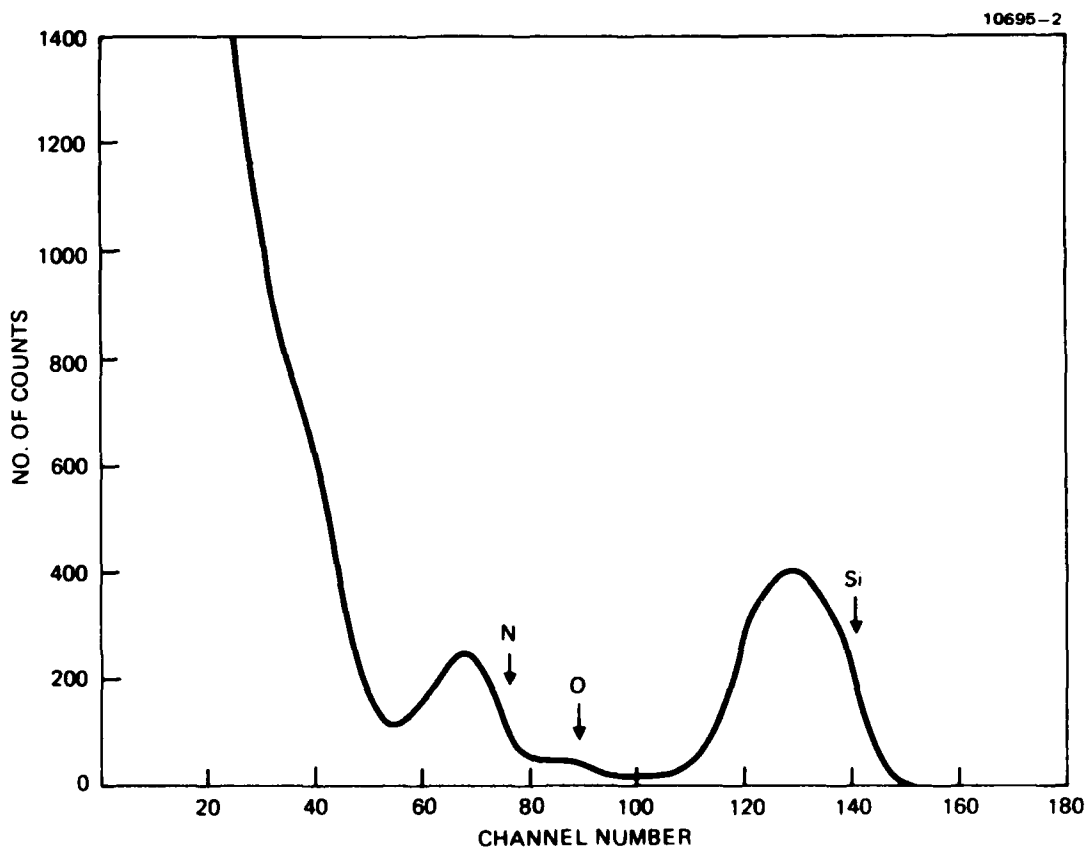


Figure 14. RBS spectra of Si_3N_4 films deposited on pyrolytically carbon film. The carbon film was supported by a silicon substrate.

10696-1

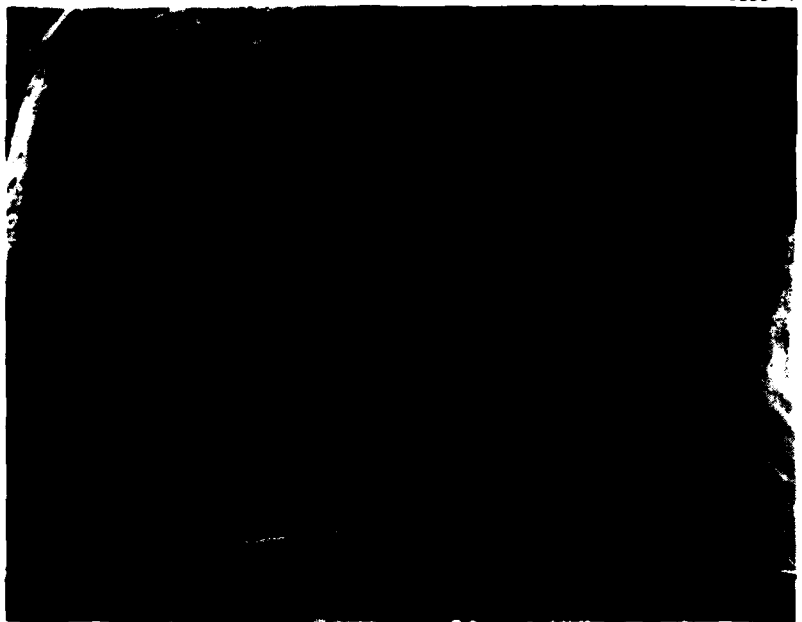


Figure 15. SEM photograph of a sample annealed with
 Si_3N_4 encapsulatn at 700°C for 30 min.

B. Be-IMPLANTED InP

Beryllium is known to be a shallow acceptor in all III-V compound semiconductors. It can be efficiently activated at relatively low temperatures. In this study, we have obtained the Be atomic distribution in as-implanted InP as well as in annealed samples. Figure 16 shows the as-implanted Be distribution at a fluence of $3 \times 10^{13} \text{ cm}^{-2}$. Three different energies were used in this study; 150 keV, 300 keV, and 600 keV. The depth scale (x-axis) was calibrated by making crater depth measurements using a Sloan-Dektak system. Since the total number of ions within the Gaussian distribution should be equal to the implanted distribution, an accurate concentration scale can be established. The impurity profiles appear to be skewed with the peak of the distribution occurring at nearly the projected range as calculated from the LSS theory. Whenever a light projectile such as Be is implanted into a substrate composed of heavy elements like InP, the resultant atomic distribution is expected to be skewed. Additional moments are required to describe it analytically. These profiles can be described by modified Pearson IV distribution which takes into account the necessary higher-order moments.

Figure 17 shows the variation in measured sheet hole concentration and hole mobility as functions of anneal temperature. The implants were performed at 300 keV to fluences of $1 \times 10^{14} \text{ cm}^{-2}$ and $3 \times 10^{13} \text{ cm}^{-2}$. The carrier concentration increases with anneal temperature, while the carrier mobility stays essentially constant. Nearly 70% of the implanted Be is electrically active in $3 \times 10^{13} \text{ cm}^{-2}$ samples, while 60% electrical activation can be achieved in $1 \times 10^{14} \text{ cm}^{-2}$ samples after annealing at 700°C for 30 min. These results are in excellent agreement with previously published data.

The Be atomic distribution in annealed samples ($1 \times 10^{14} \text{ cm}^{-2}$, 650 and 700°C anneals) are shown in Figure 18. For comparison, the unannealed profile is also shown. This figure clearly demonstrates that considerable redistribution of Be takes place at high concentrations, even at 650°C. The redistribution effects reported here are qualitatively similar to the behavior of ion-implanted Be in GaAs. The threshold concentration and anneal temperature at which redistribution effects occur in InP have not yet been established. These studies are presently being carried out.

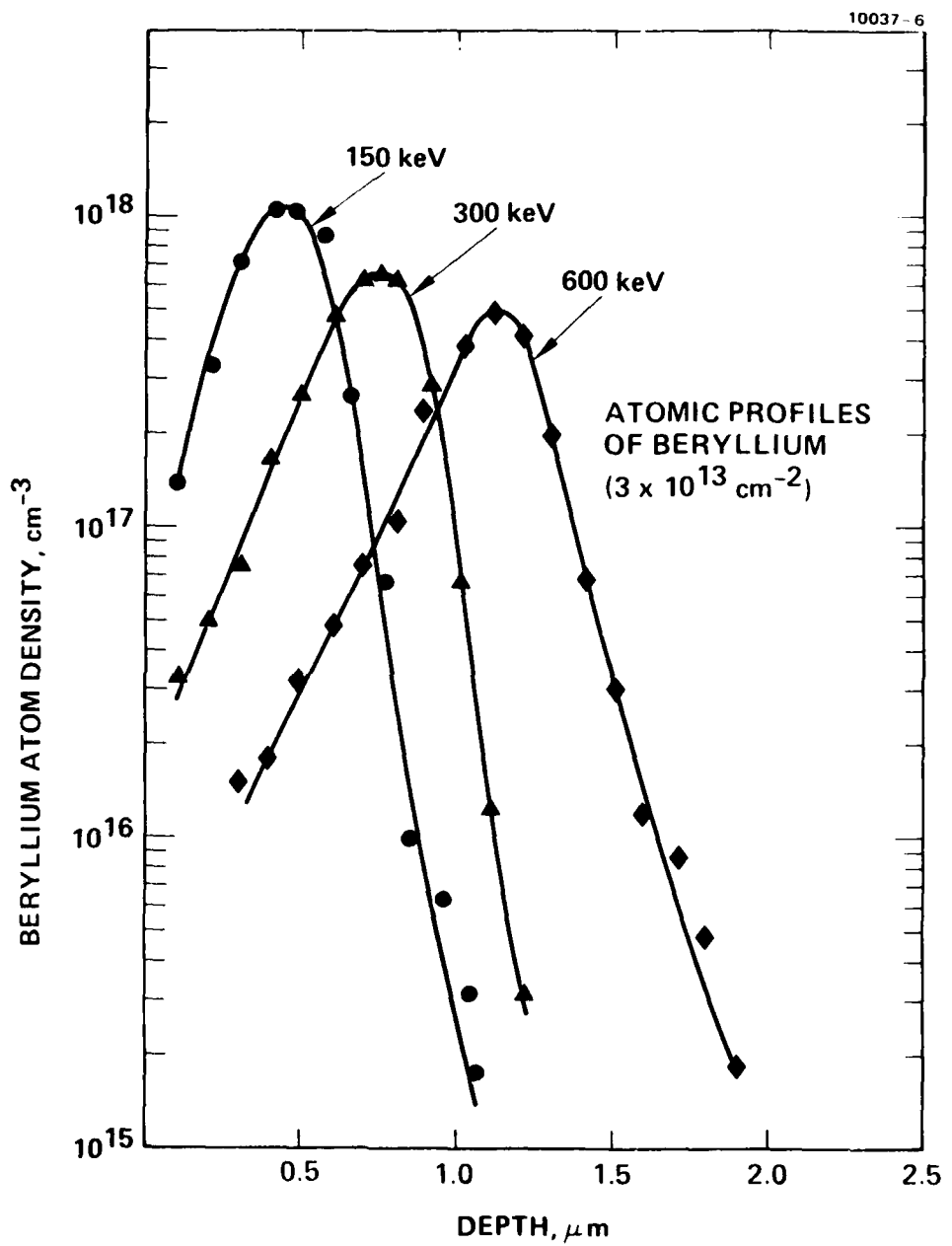


Figure 16. Atomic distribution of ion-implanted Be in InP. The implant energies were 150 keV, 300 keV and 600 keV with an implant fluence of $3 \times 10^{13} \text{ cm}^{-2}$.

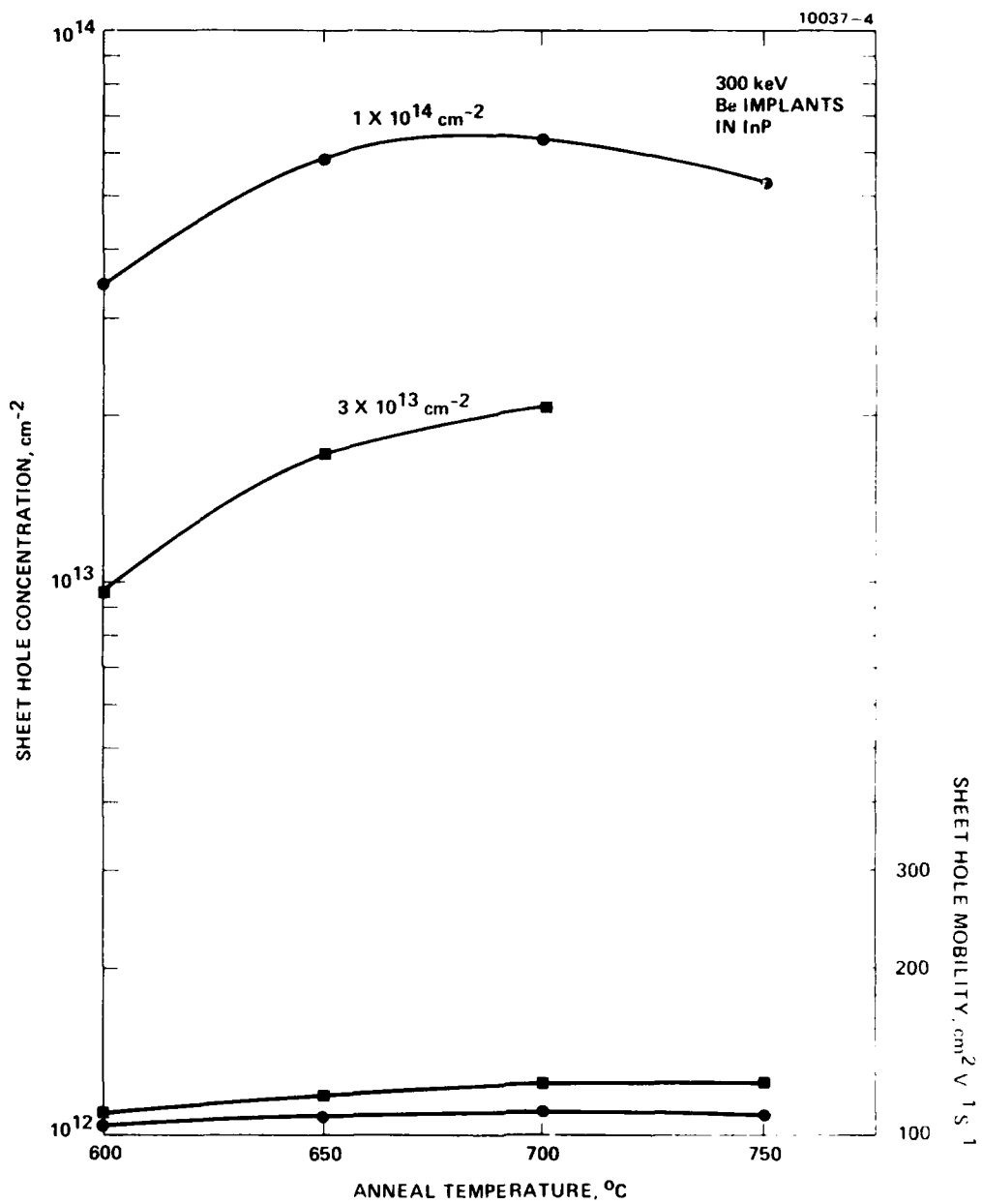


Figure 17. Sheet hole concentration and hole mobility as functions of anneal temperature for InP samples implanted with 300 keV Be.

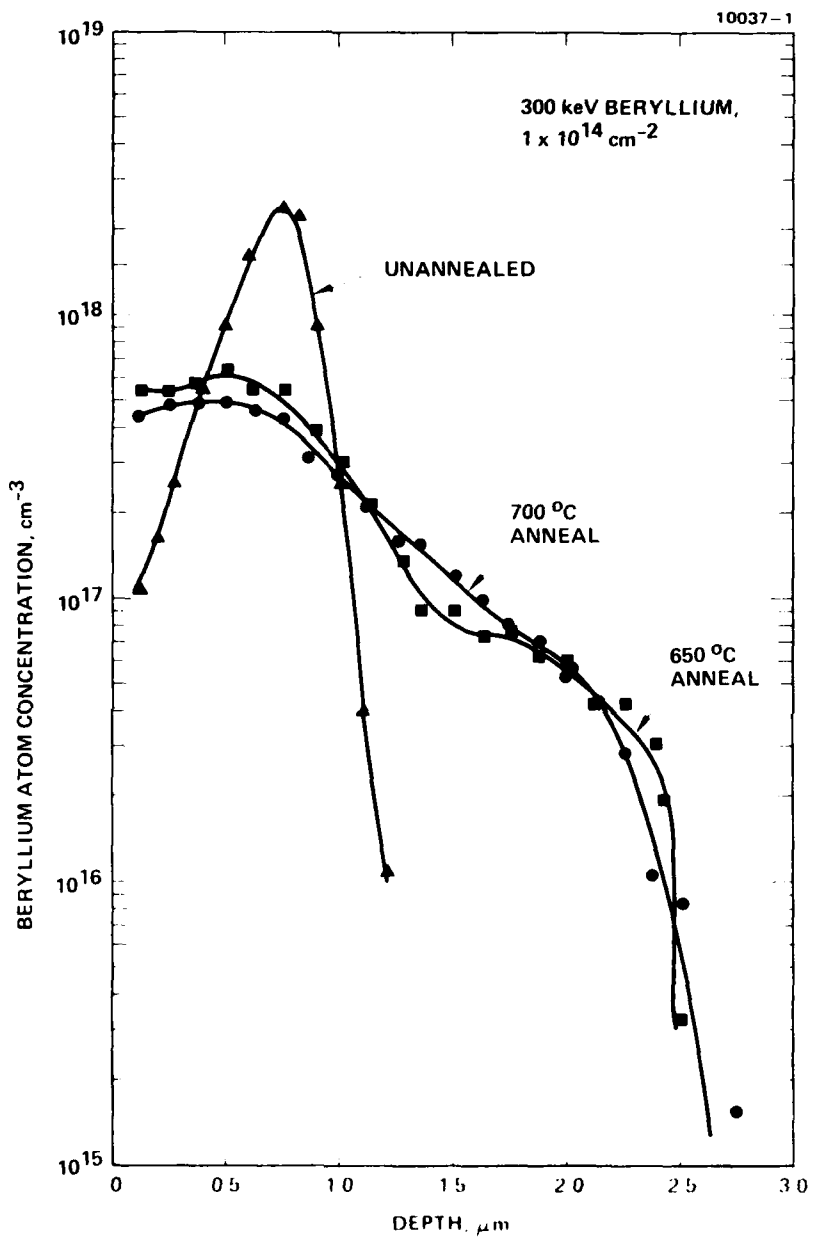


Figure 18. Atomic distribution of ion-implanted Be obtained from unannealed and annealed InP samples showing effects of drastic redistribution.

We have also studied the properties of InP samples capless annealed, using our patented melt-controlled ambient technique. MCAT was demonstrated using Hughes internal funds and was carefully evaluated for annealing GaAs under an AFOSR contract. The process uses the infinite solution growth apparatus described in Section 2. To prevent the sample from coming into physical contact with the solution, a specially designed sample holder is used that provides a liquid-tight cover. The cover, however, is not vapor tight. The interior of the sample holder has been opened to the melt before the sample is introduced into it. The high-purity graphite is porous to the melt vapors. These factors result in a stable, controlled ambient that is presented to the sample being annealed.

The data from MCAT-annealed samples show that high carrier activation can be achieved. The carrier mobility is, however, disappointingly low; in fact, the mobility in MCAT-annealed samples is almost an order of magnitude lower than in comparable samples annealed with an encapsulant. The observed reduction in mobility is probably the result of large number of phosphorus vacancies created during the annealing process. With MCAT, both the sample and the holder are held in the hydrogen ambient for a considerable length of time before being introduced into the melt. This is necessary to prevent crystallization around the cold sample holder. Since the vapor pressure of phosphorus is high, we believe that considerable surface degradation takes place during this pre-anneal treatment. To test this hypothesis, some samples were annealed with a silox encapsulant in the MCAT system. The carrier mobility in these samples is comparable to that in samples annealed with an encapsulant in a conventional fashion.

The table also presents data obtained from samples annealed in a flowing phosphine ambient. Samples annealed in an ambient of 0.1 at .% phosphine showed severe surface degradation at 640°C. However, samples annealed in 1 at .% phosphine showed no visible surface degradation, and the electrical properties of these layers were comparable to those of layers annealed with PSG encapsulation. These results demonstrate that a high degree of vapor phase control is necessary to capless anneal InP. These preliminary results have been recently reported,^{7,8} and are in good agreement with previously published data.

C. Si-IMPLANTED InP

We have evaluated the electrical properties and atomic distribution of silicon-implanted InP. Figure 19 illustrates the variation in carrier concentration and carrier mobility as a function of anneal temperature. The implant dose covered in this study ranged from $5 \times 10^{12} \text{ cm}^{-2}$ to $1 \times 10^{14} \text{ cm}^{-2}$. The implant energy was kept at 300 keV. The measured sheet carrier concentration increases with anneal temperature over the range studied. In the case of low fluence implanted samples ($< 3 \times 10^{13} \text{ cm}^{-2}$) more than 80% of the implanted ions were electrically activated on annealing at 750°C. In the case of high fluence implanted samples ($> 6 \times 10^{13} \text{ cm}^{-2}$), the measured sheet carrier concentration appeared to saturate at $5 \times 10^{13} \text{ cm}^{-2}$. As expected, the low fluence implanted samples exhibited higher carrier mobilities. For samples implanted to $\sim 5 \times 10^{12} \text{ cm}^{-2}$ and annealed at 750°C, the measured mobility was $\sim 2,900 \text{ cm}^2 \text{V}^{-1} \text{sec}^{-1}$, while $6 \times 10^{13} \text{ cm}^{-2}$ and $1 \times 10^{14} \text{ cm}^{-2}$ implanted samples had mobilities of $1,100 \text{ cm}^2 \text{V}^{-1} \text{sec}^{-1}$.

This information is summarized in Figure 20, where the measured sheet carrier concentration is plotted as a function of the ion dose. The 100% (complete) activation line is also shown in this figure for comparison. The three solid curves represent the results after annealing at 650, 700, and 750°C. As seen from this figure, for doses ranging from $8 \times 10^{12} \text{ cm}^{-2}$ to $4 \times 10^{13} \text{ cm}^{-2}$, almost complete activation can be achieved following annealing at 750°C. We are presently evaluating the electrical properties of low fluence ($< 5 \times 10^{12} \text{ cm}^{-2}$) implanted samples in order to extend the range shown in Figure 20.

The Si atomic profiles obtained by SIMS analysis from samples implanted with 300 keV Si^+ to different fluences and annealed at 650°C for 30 min are shown in Figure 21. It appears that there is very little diffusion of silicon at this temperature. The profiles are in reasonable agreement with the LSS theoretical predictions for GaAs.

D. DAMAGE STUDIES

It has been demonstrated that amorphous layers formed by ion implantation can be annealed in silicon by a solid-phase epitaxial growth process at

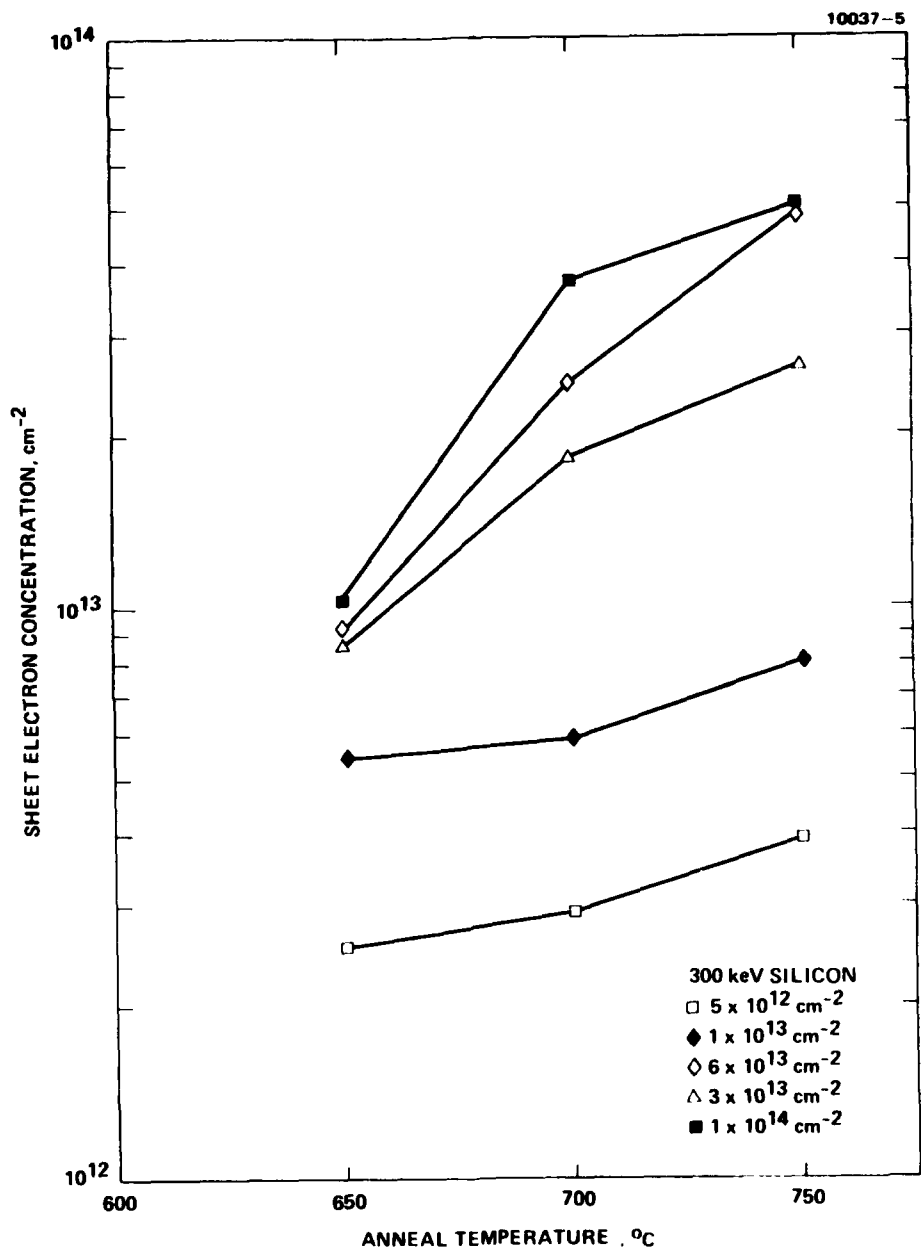


Figure 19. Sheet electron-concentration as a function of anneal temperature for InP samples implanted with 300 keV silicon to fluences indicated in figure.

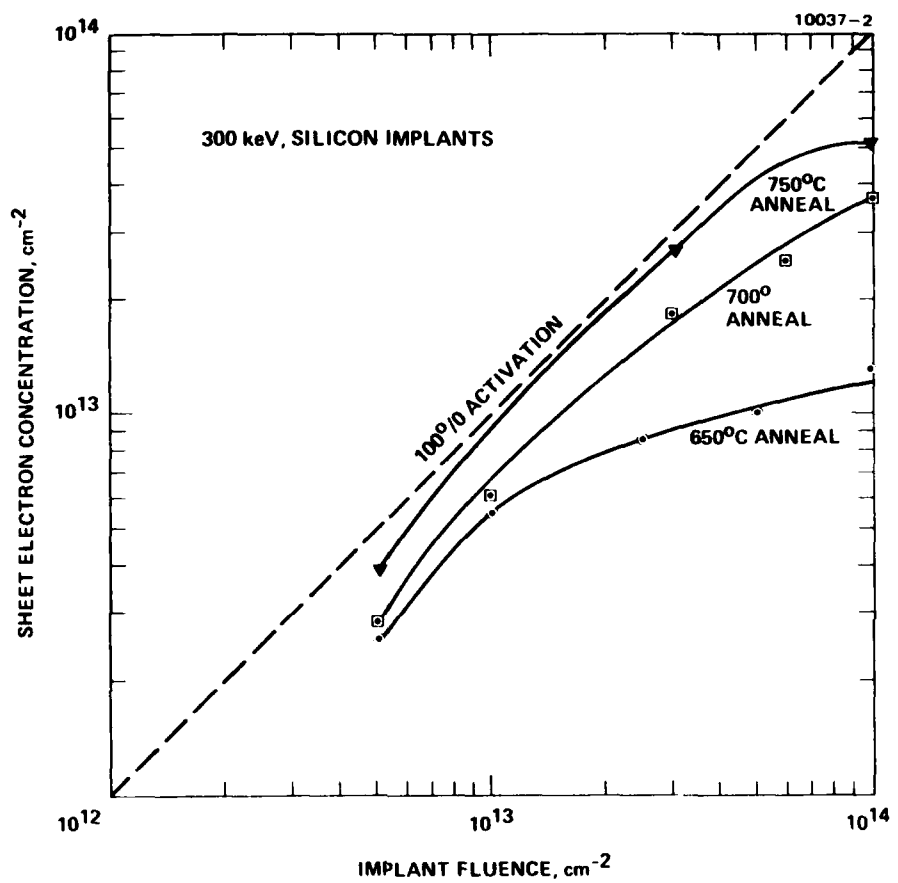


Figure 20. Sheet electron concentration as a function of implant fluence for 300 keV Si-implanted InP samples.

~500°C. The resultant crystalline layers exhibited acceptable electrical properties. In our internally funded investigations, we observed that amorphous layers can be formed in GaAs at low implant fluences ($\sim 2 \times 10^{13} \text{ cm}^{-2}$ 100 keV Si⁺) provided the implants were performed at low temperature (-100°C or lower). Such layers can be epitaxially regrown at temperatures as low as 200°C. Such a recrystallization process (if it exists in InP) may be invaluable since the anneal temperature will be well below the dissociation temperature of the material. To investigate this, we have initiated a series of experiments to analyze the implant-induced damage in InP using the Rutherford backscattering technique. The results obtained from samples implanted at room temperature by RBS analysis are discussed below. More detailed studies on samples implanted at room temperature and low temperature will be performed on the second phase of this program.

E. RUTHERFORD BACKSCATTERING STUDIES

The backscattering studies were performed by using a system developed at HRL. The system is capable of operating at 150 dV. H⁺, He⁺, and He⁺⁺ ions can be used to perform the RBS analysis. The use of He⁺⁺ permits the experiments to be performed at 300 keV. The ion optics in the system provide a well-collimated beam with beam divergence of less than 0.1°. The target to be analyzed is mounted on a goniometer. By using this goniometer, we can align the sample with respect to the beam to within 0.02°. The analysis is performed by detecting the backscattered particles with a cooled surface barrier detector. A Canberra model 80 multichannel analyzer, in conjunction with a DEC PDT-11 computer system, is used to analyze the pulses obtained from the detector and results in the display of the number of backscattered particles as a function of energy.

The analysis of the data allows us to determine the degree of crystallinity or damage formation, the depth of the damaged layer (provided it is not much deeper than 2,000 Å from the surface) and the location of dopants in the lattice by performing channel measurements, provided the dopant atoms are more massive than the substrate atoms.

A sample of InP was implanted with Si^+ at 100 keV. By using appropriate metal masks, different portions of the sample were implanted to fluences ranging from $2 \times 10^{12} \text{ cm}^{-2}$ to $6 \times 10^{13} \text{ cm}^{-2}$. The RBS spectra obtained from these regions as well as from a non-implanted region are shown in Figure 22. The implants were carefully controlled and were performed at the same dose rate to ensure that the damage versus dose curve can be constructed. The damage as measured by the number of counts at the point of maximum damage is plotted as a function of implant fluence in Figure 23.

We will use the RBS technique to evaluate the damage production as functions of implantation temperature and dose and the reordering of such layers as a function of anneal temperature. After establishing the temperature to anneal the damage, we will evaluate the electrical properties of such recrystallized layers.

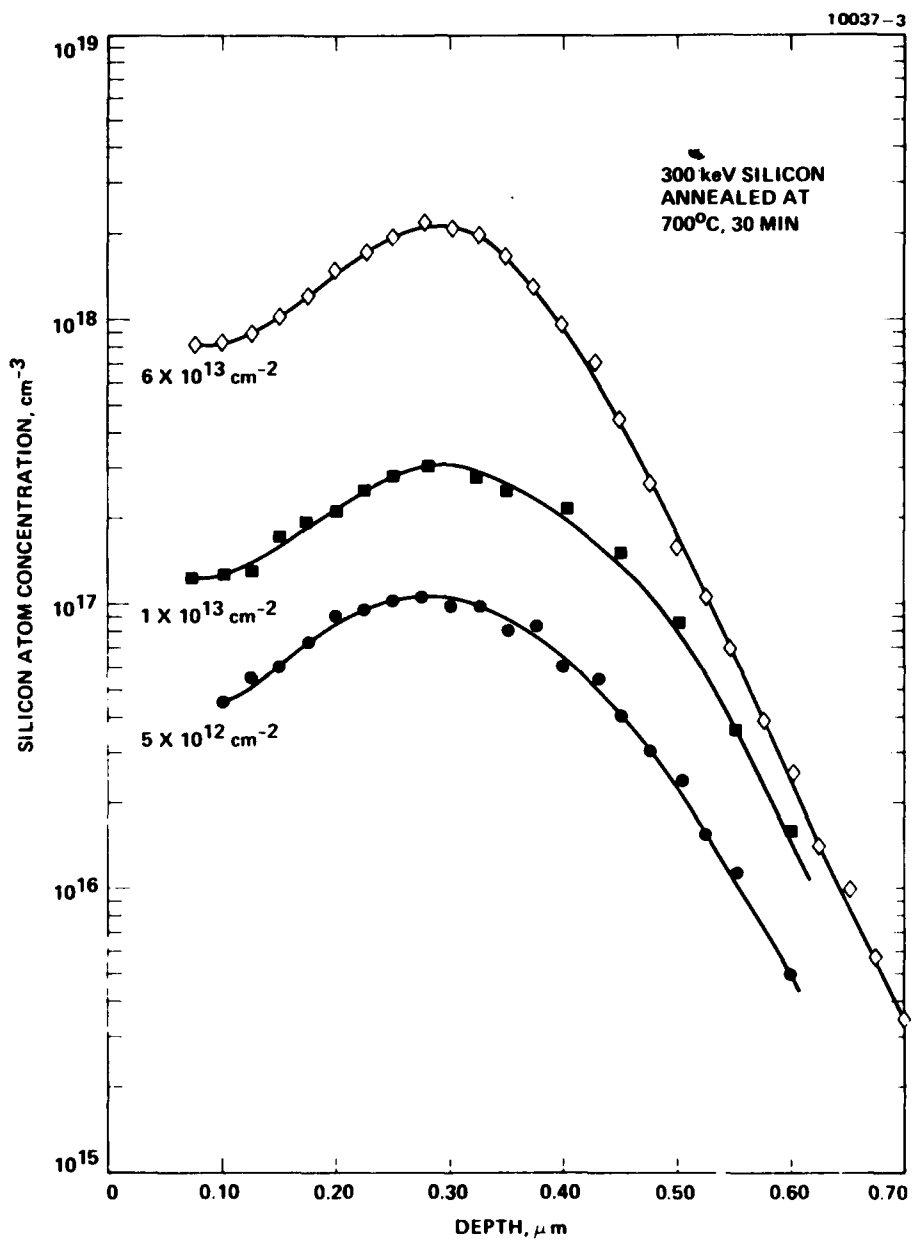


Figure 21. Atomic distribution obtained from Si implanted and annealed InP samples.

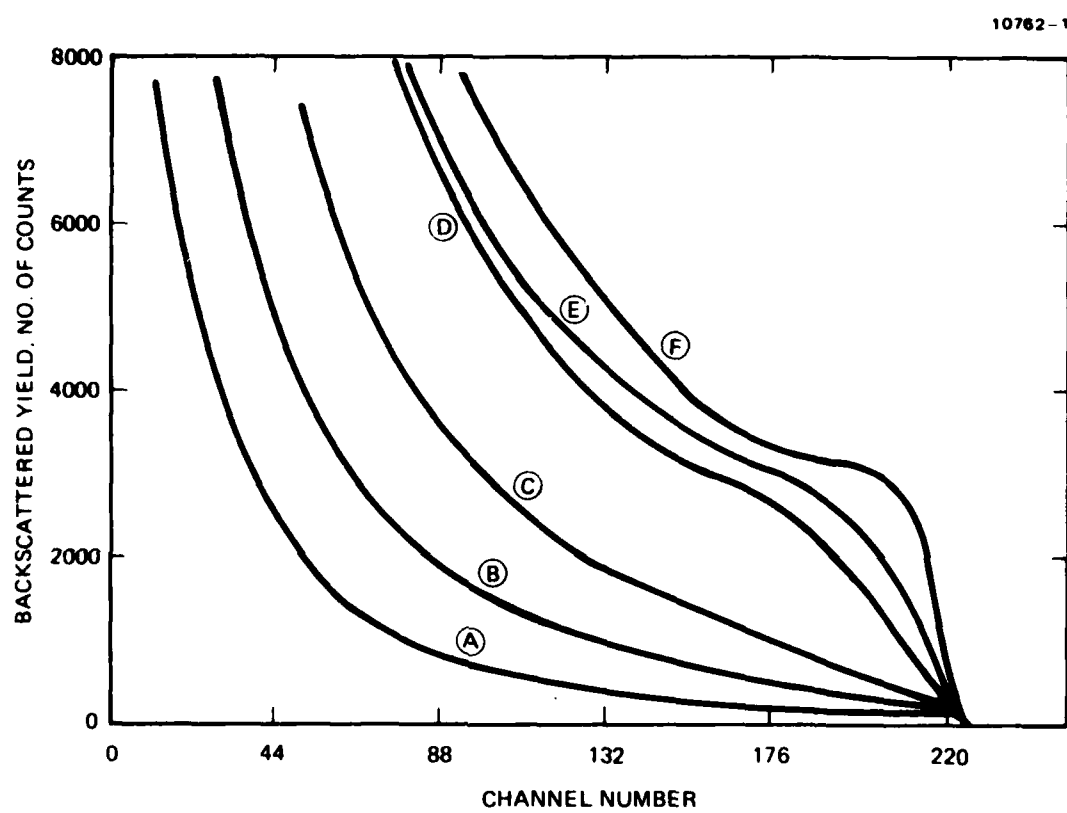


Figure 22. RBS spectra obtained from InP samples.

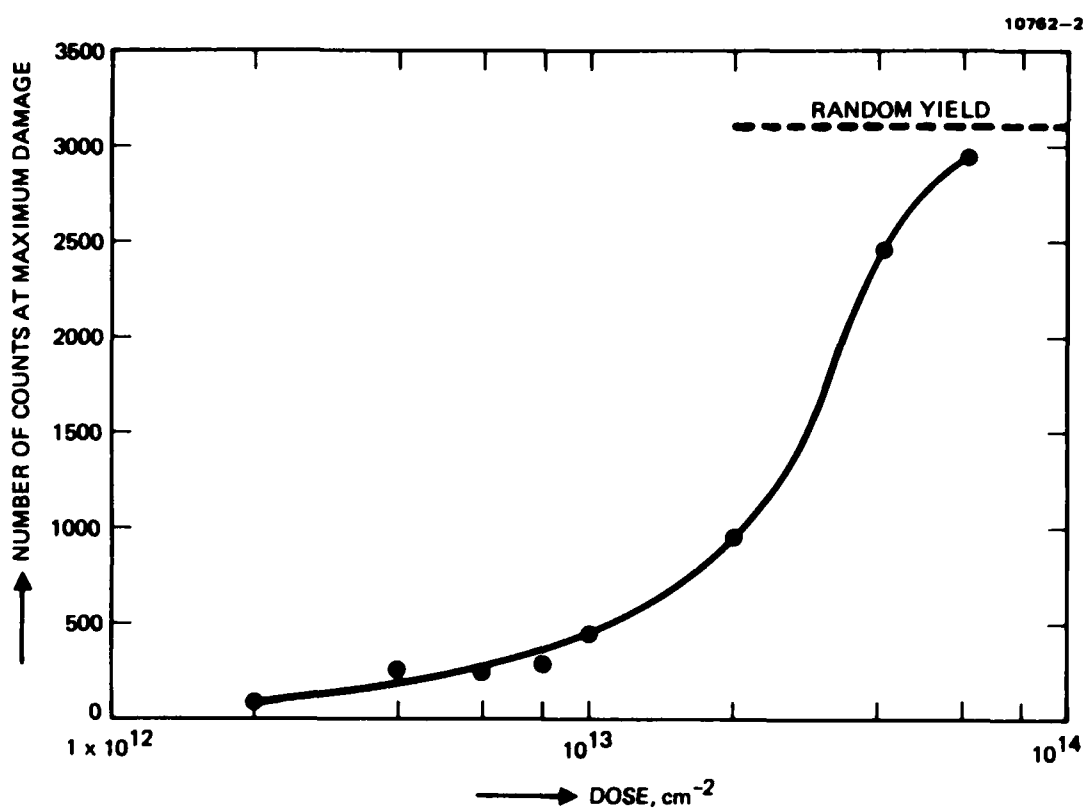


Figure 23. Dose versus damage curve for InP implanted with silicon at room temperature.

SECTION 5

SUMMARY

In the area of epitaxial growth, high-purity n-type layers with carrier concentrations of $\sim 3 \times 10^{15} \text{ cm}^{-3}$ and room temperature mobilities $4,500 \text{ cm}^2 \text{V}^{-1} \text{-sec}^{-1}$ with excellent surface morphology have been reproducibly grown using the infinite solution growth technique. To grow layers with such properties, it is necessary to introduce small quantities ($\sim 1 \text{ ppm}$) of water vapor in to the growth ambient. The presence of such small quantities of water vapors suppresses the reduction of quartz to silicon by the hydrogen present in the growth ambient. The silicon doping of the solution and of the epitaxial layers is minimized by the addition of water vapor. Preliminary Auger electron spectroscopy (AES) and secondary ion mass spectrometry (SIMS) data show that the epitaxial layers grown in the absence of water vapor contain a higher concentration of silicon compared to the layers grown in the presence of water vapor. The SIMS data also reveal the presence of sulfur in the epitaxial layers. Thus the electrical properties of the epitaxial layers result from an interaction between the residual donors sulfur and silicon and the water vapor present in the growth ambient.

We have performed preliminary studies on ohmic-contact formation to p- and n-type InP. Au:Zn and Au:Ge/Ni appear to be the appropriate metals to use for ohmic contacts to p- and n-InP, respectively. We have determined that power densities higher than $5 \times 10^4 \text{ W/cm}^2$ result in permanent crystal damage to InP. Consequently, cw laser-annealed ohmic contacts will have to be made at power densities lower than $5 \times 10^4 \text{ W/cm}^2$.

Severe surface degradation was observed in ion-implanted InP samples and annealed with SiO_2 encapsulant. The loss of phosphorus underneath the oxide appears to be the dominant mechanism for this surface degradation. The effect can be minimized by encapsulating the sample with phosphosilicate glass during the anneal. The studies discussed in this report clearly demonstrate that PSC

films containing between 5 to 8 at.% phosphorus can be used to anneal InP at 750°C. Efficient electrical activation with acceptable mobilities can also be achieved by performing the anneals in a flowing phosphine ambient. No surface degradation was observed when the samples were annealed at 640°C in an ambient of 1% phosphine. Higher concentrations of phosphine may be necessary to anneal InP at higher temperatures.

In the case of Be-implanted samples, more than 60% of the implanted Be became active over a range of doses ($1 \times 10^{13} \text{ cm}^{-2}$ to $1 \times 10^{14} \text{ cm}^{-2}$) after annealing at temperatures of 700°C or higher. Secondary ion mass spectrometry studies demonstrate that while the as-implanted impurity profile is approximately Gaussian, Severe redistribution effects occur at concentrations higher than $\sim 8 \times 10^{17} \text{ cm}^{-3}$. Detailed studies are being carried out.

In the case of silicon-implanted samples, almost complete activation of the implanted dopants with acceptable electron mobilities were obtained over doses ranging from $\sim 4 \times 10^{12} \text{ cm}^{-2}$ to $5 \times 10^{13} \text{ cm}^{-2}$ after annealing at 750°C. The percentage of activation drops off at both higher and lower fluences. Preliminary SIMS measurements indicate that no significant diffusion of the implanted silicon occurs.

The damage created in InP by silicon implantation has been studied by Rutherford backscattering analysis. The recovery of this damage as a function of anneal temperature is currently being studied.

REFERENCES

1. M.A. Littlejohn, J.R. Hauser, T.H. Glisson, D.K. Ferry, and J.W. Harrison, Solid-State Electron. 21, 107 (1978).
2. S.H. Groves and M.C. Plonko, Institute of Physics Conf., Series No. 45, 71 (1978), and reference therein.
3. R.C. Clarke, Institute of Physics Conf., Series No. 45, 19 (1978), and references therein.
4. J.P. Duchemin, M. Bonnet, G. Beuchet, and F. Koelsch, Institute of Physics Conf., Series No. 45, 10 (1978) and references therein.
5. L.M. Fraas and K. Zanio, J. Electronic Materials 7, 221 (1978).
6. J.H. McFee, B.I. Miller, and K.J. Bachman, J. Electrochem. Soc 124, 259 (1977).
7. K.V. Vaidyanathan, C.L. Anderson, H.L. Dunlap, and D.E. Holmes, to be published in J. Nuclear Instruments and Methods.
8. C.A. Armiento, J.P. Donnelly, and S.H. Groves, Appl. Phys. Lett. 34, 229 (1979).
9. J.P. Donnelly and C.E. Hurwitz, Solid-State Electron. 21, 475 (1978).
10. D. Eirug Davies, J.P. Lorenzo, and T.G. Ryan, Solid-State Electron. 21, 981 (1978).

